ORIGINAL ARTICLE

Petrographical and geochemical constraints on carbonate diagenesis in an epeiric platform deposit: Late Cretaceous Bagh Group in central India

Dhiren K. Ruidas[1] · Fotini A. Pomoni-Papaioannou[2] · Santanu Banerjee[1] · Tapas Kumar Gangopadhyay[3]

Abstract

A combined facies, petrography and isotope geochemistry reveal an extensive pedogenic alteration of platform carbonate deposits of the Upper Cretaceous Bagh Group in the western Narmada basin in central India. The highly fossiliferous carbonate sequence of the Bagh Group consists of two formations, the Nodular Limestone at the base, and the Bryozoan Limestone Formation at top. The Nodular Limestone Formation comprises primarily of mudstone and wackestone, with relics of bioclasts such as gastropods, echinoderms, molluscs, forams and calcispheres, reflecting a low-energy supratidal to upper intertidal environment of deposition. Prolonged pedogenesis leads to pervasive micritization, brecciation, desiccation and recrystallization. The overlying Bryozoan Limestone, dominated by packstone and planar laminated rudstone with bryozoans, gastropods, echinoderms/echinoid spines, and molluscs, indicates deposition within the lower intertidal environment with moderately high-energy conditions. Abundant meniscus cement and biomolds suggest meteoric vadose diagenetic modification, whereas, intense secondary micritization of sediments indicates prolonged calichification. The $\delta^{13}C$ and $\delta^{18}O$ ratios of both Nodular Limestone and Bryozoan Limestone formations are depleted than the normal marine values, indicating an extensive diagenetic resetting of the carbonates. While the meteoric cement is depleted in both $\delta^{13}C$ and $\delta^{18}O$ ratio, the burial cement shows a decrease of $\delta^{18}O$ at constant $\delta^{13}C$. The pedogenetic horizons within the Bagh carbonates bear subtle evidence of subaerial exposures within the overall transgressive Bagh Group. A glauconite bed at the upper part of the Bryozoan Limestone Formation marks the top part of the transgressive deposit.

Keywords Bagh group · Pedogenesis · Stable isotopes · Meteoric diagenesis · Cathodoluminescence · Late Cretaceous · Epeiric platform

Abbreviation
VPDB   Vienna-Pee Dee Belemnite

✉ Santanu Banerjee
  santanu@iitb.ac.in

1   Department of Earth Sciences, Indian Institute
    of Technology Bombay, Powai, Mumbai 400076, India

2   Faculty of Geology and Geoenvironment, School of Science,
    National and Kapodistrian University of Athens (NKUA),
    Athens University Campus, 157 84 Athens, Greece

3   Indian Institute of Engineering Science and Technology,
    Shibpur, Howrah 711103, India

Introduction

A significant interval of the Cretaceous Period corresponds to expansive epeiric seas that formed vast carbonate platforms (Tucker and Wright 1990; Sanders 1998; Gómez-Gras and Alonso-Zarza 2003; Coimbra et al. 2016, 2017; Wilmsen et al. 2018). Shallow water condition with apparently restricted water circulation is characteristic of epeiric seas. The epeiric platform carbonates provide valuable insights for the reconstruction of sea level and climate of past and by recording the subtle breaks in sedimentation within an otherwise continuous shallow marine sequence. The subaerial exposure associated with the depositional breaks in carbonate succession causes diagenetic modification of the metastable sediments. Diagenetic overprinting alters carbon and oxygen isotope ratios of these shallow marine carbonate successions significantly (Joachimski 1994; Buonocunto et al. 2002). A detailed investigation involving field,

petrographical and geochemical approaches, is necessary to characterize the subaerial exposure surfaces within marine carbonates (Meyers and Lohmann 1985; Goldstein 1988; Saller and Moore 1989; Alonso-Zarza et al. 1998, 1999; Gómez-Gras and Alonso-Zarza 2003; Budd et al. 2002).

The Upper Cretaceous sedimentary succession of the Narmada Basin in central India retains the crucial records of the paleogeographic evolution and sea level cycles before the onset of the globally significant Deccan volcanic eruptions. The Bagh Group of the Narmada Basin in central India represents the deposits of the Late Cretaceous marine inundation of the Indian subcontinent. It has received considerable attention for its rich fossil assemblage, including echinoderm (Chiplonkar 1937), bivalve (Chiplonkar and Badve 1976), bryozoa (Guha 1975), ammonite (Kennedy et al. 2003; Gangopadhyay and Bardhan 2000; Jaitly and Ajane 2013 and many others). While sedimentological studies remain focused on the clastic sequence of the Narmada Basin (Singh and Dayal 1979; Bose and Das 1986; Bhattacharya and Jha 2014; Jha et al. 2017), the carbonate deposits are largely ignored. The main objective of this paper is to present depositional and diagenetic histories of the Bagh Group of carbonates in the western part of the Narmada Basin. Further, we investigate the relationship between the depositional environments, diagenesis and stable isotope ratios of carbonates. We present a detailed interpretation of facies and paleo-environment based on field and petrographic investigation and integrate the data with cathodoluminescence pattern and stable isotope ratios of carbonates for a better understanding of the diagenetic history.

Geological and stratigraphic background of Bagh Group

The mixed carbonate–siliciclastic sequence of the Bagh Group comprises Nimar Sandstone, Nodular Limestone and Bryozoan Limestone formations in ascending order of succession. The Bagh Group of rocks is exposed as isolated inliers surrounded by Deccan Traps in west-central India (Fig. 1). The Bagh Group represents the deposits in an easterly transgressing arm of the paleo-Tethys. It crops out at the western part of the ~1200 km long Narmada basin.

The Bagh Group unconformably overlies the Precambrian basement and it grades to fluvio-marine Lameta Formation (Tripathi 1995, 2006; Tripathi and Lahiri 2000). The carbonate deposit of the Bagh Group overlies the siliciclastic Nimar Formation and consists of two formations, the Nodular Limestone at the base and the Bryozoan Limestone at the top (Fig. 2). The upper contact of the Bagh Group is
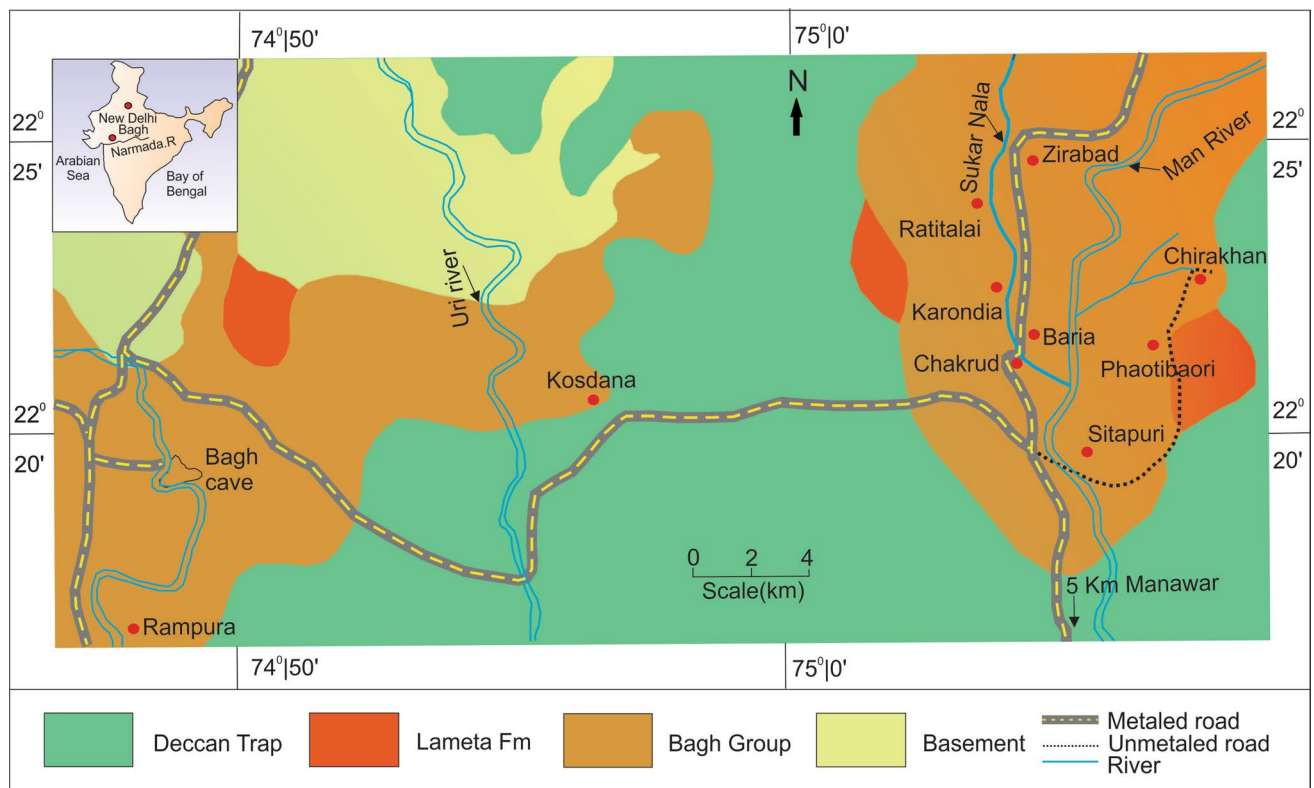

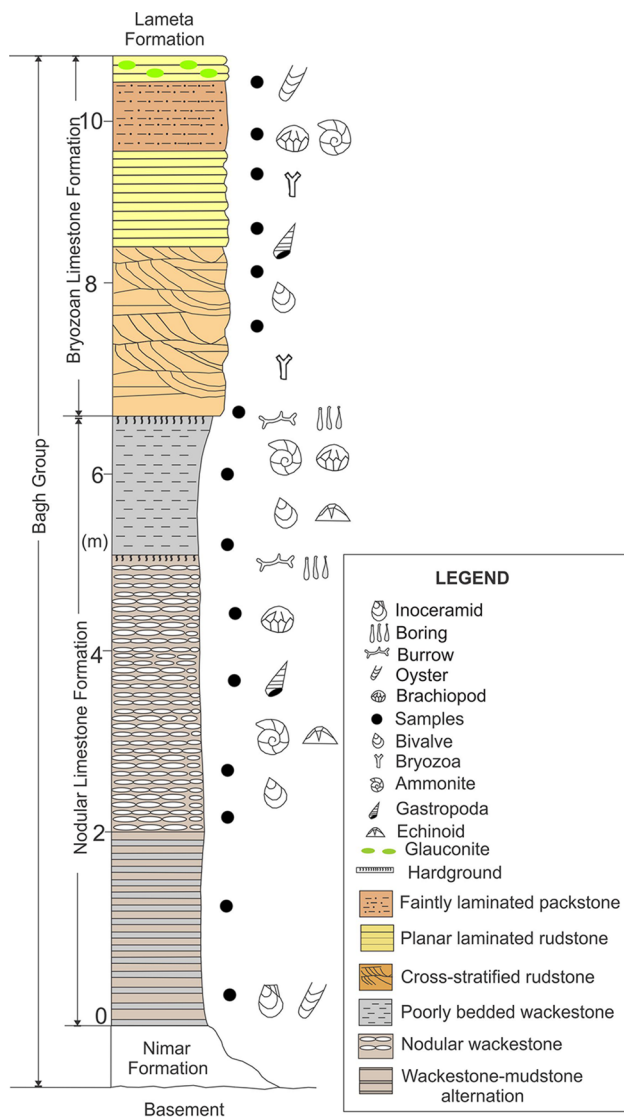**Fig. 1** Geological map showing locations of the study area

Fig. 2 Lithocolumn showing the general stratigraphy of the Bagh Group, constituent facies and fossils

controversial. Some authors have recorded an unconformable contact between the marine originated Bagh Group and the continental deposits of the Lameta Formation (Tripathi 2006). However, in the western Narmada basin, the marine sediments of the Bagh Group grade upward to estuarine deposits of the Lameta Formation (Ahmad and Akhtar 1990; Tandon 2000; Bansal et al. 2018, 2019). Sedimentological, paleontological, and ichnological data obtained from the Bagh Group (Singh and Srivastava 1981; Jaitly and Ajane 2013; Bhattacharya and Jha 2014; Jha et al. 2017). The best exposures of the Bagh Group occur mainly on the northern flank of the river Narmada around Chakroad, Kasdana, Baria, Mohi, Karondia, Zeerabad, Phutlibaori, Sitapura and Rampura (Fig. 1). Biostratigraphic investigations provide Cenomanian to Turonian age for the Bagh Group

(Kumar et al. 2018). Recently Kumar et al. (op. cit.) provided Cenomanian, Turonian and Coniacian ages for Nimar Sandstone, Nodular Limestone and Bryozoan Limestone, respectively based on ammonite biostratigraphy (Table 1).

Methodology

The current study involves a detailed field investigation of the Bagh Group in Dhar district, central India that covered sections around Man River, Zirabad, Chakroad, Mohi, Ratitalai, Rampura, Karondia, Kosdana, and Phutlibaori (Fig. 1). We collected around 40 samples from ten localities and recorded their precise stratigraphy. Samples were examined using Leica DM 4500P polarizing microscope connected to a Leica DFC420 camera. Thin sections were examined using an optical cathodoluminescence system (CL8200Mk5-2) at 392–400 µA and 17.2 kV in the Sedimentology Laboratory of Jadavpur University. Stable carbon and oxygen isotope ratios of the carbonates were measured in the Stable Isotope Laboratory of the Indian Institute of Science Education and Research, Kolkata. Powdered samples were obtained from fresh surfaces of micritic carbonates and different generations of spars using a microdrilling device capable of high-resolution milling (Micro-Mill) in the Stable Isotope Laboratory of the Indian Institute of Science Education and Research, Kolkata. Approximately 80–100 µg powdered carbonate samples were inserted in glass vials and reacted with 100% phosphoric acid at 80 °C using a KIEL IV online automatic carbonate preparation device connected to MAT 253 mass spectrometer in dual inlet mode. A calcite standard (NBS18) and an internal standard (Z-Carrara) were run to monitor the instrumental drift. All carbon and oxygen isotope ratios are reported using the delta (δ) notation in per mil (‰) relative to the Vienna Pee Dee Belemnite (VPDB). The analytical reproducibility of the standard is $\pm 0.3‰$ (1σ) for $\delta^{13}C$ and $\pm 0.05‰$ (1σ) for $\delta^{18}O$.

Results

We present facies analysis, luminescence characteristics and stable isotope ratios of constituent carbonates of the Bagh Group in the following discussion.

Facies analysis

The Nodular Limestone Formation overlies the fluvio-marine siliciclastics of the Nimar Formation. Description and interpretation of constituent facies of the Nodular Limestone and Bryozoan Limestone are provided below.

Table 1 Stable isotopic ratios for the Nodular Limestone Formation and the Bryozoan Limestone Formation

Facies name	Sample no	Content	$\delta^{18}O‰$ (VPDB)	$\delta^{13}C‰$ (VPDB)
Planar laminated rudstone	BG/ND/122	Cement	− 5.3	− 1.1
Planar laminated rudstone	BG/ND/121	Cement	− 6.2	− 2.1
Planar laminated rudstone	BG/ND/120	Cement	− 4.6	0.2
Planar laminated rudstone	BG/ND/119	Cement	− 6.6	− 1.9
Planar laminated rudstone	BG/ND/118	Cement	− 5.8	− 1.2
Planar laminated rudstone	BG/ND/117	Cement	− 5.9	− 2.6
Planar laminated rudstone	BG/ND/116	Cement	− 6.8	− 2.5
Planar laminated rudstone	BG/ND/115	Matrix	− 8.1	− 3.9
Planar laminated rudstone	BG/ND/114	Cement	− 8.1	− 3.6
Planar laminated rudstone	BG/ND/113	Matrix	− 9.2	− 4.0
Planar laminated rudstone	BG/ND/112	Matrix	− 8.2	− 3.3
Planar laminated rudstone	BG/ND/111	Matrix	− 8.5	− 3.6
Planar laminated rudstone	BG/ND/110	Cement	− 8.5	− 3.4
Faintly laminated packstone	BG/ND/109	Matrix	− 11.7	− 2.1
Faintly laminated packstone	BG/ND/108	Cement	− 12.5	− 1.9
Faintly laminated packstone	BG/ND/107	Cement	− 9.5	− 2.0
Faintly laminated packstone	BG/ND/106	Cement	− 7.0	− 1.5
Faintly laminated packstone	BG/ND/105	Cement	− 6.7	− 0.9
Faintly laminated packstone	BG/ND/104	Cement	− 6.2	− 1.1
Faintly laminated packstone	BG/ND/103	Cement	− 6.3	− 1.2
Faintly laminated packstone	BG/ND/102	Matrix	− 6.9	− 2.4
Faintly laminated packstone	BG/ND/101	Cement	− 7.9	− 3.1
Faintly laminated packstone	BG/ND/100	Matrix	− 9	− 2.5
Faintly laminated packstone	BG/ND/099	Matrix	− 6.9	− 1.6
Cross-stratified rudstone	BG/ND/098	Matrix	− 9.2	− 3.4
Cross-stratified rudstone	BG/ND/097	Cement	− 23.4	− 5.3
Cross-stratified rudstone	BG/ND/096	Cement	− 7.5	− 1.9
Cross-stratified rudstone	BG/ND/095	Cement	− 7.0	− 2.0
Cross-stratified rudstone	BG/ND/094	Cement	− 9.4	− 2.8
Cross-stratified rudstone	BG/ND/093	Cement	− 10.4	− 2.1
Cross-stratified rudstone	BG/ND/092	Cement	− 9.1	− 2.9
Cross-stratified rudstone	BG/ND/091	Matrix	− 10.6	− 3
Cross-stratified rudstone	BG/ND/090	Cement	− 12	− 2
Cross-stratified rudstone	BG/ND/089	Matrix	− 10.7	− 1.5
Cross-stratified rudstone	BG/ND/088	Cement	− 10.2	− 3.7
Cross-stratified rudstone	BG/ND/087	Matrix	− 5.9	− 2.1
Cross-stratified rudstone	BG/ND/086	Matrix	− 5.3	− 1.1
Cross-stratified rudstone	BG/ND/085	Cement	− 4.4	− 0.3
Cross-stratified rudstone	BG/ND/084	Cement	− 4.7	− 1.3
Cross-stratified rudstone	BG/ND/083	Cement	− 12.2	− 1.9
Cross-stratified rudstone	BG/ND/082	Cement	− 5.9	− 2.3
Cross-stratified rudstone	BG/ND/081	Matrix	− 6.8	− 1.8
Cross-stratified rudstone	BG/ND/080	Matrix	− 5.8	− 1.3
Cross-stratified rudstone	BG/ND/079	Matrix	− 18	− 1
Poorly bedded wackestone	BG/ND/078	Cement	− 6.8	− 3.6
Poorly bedded wackestone	BG/ND/077	Cement	− 8.1	− 0.9
Poorly bedded wackestone	BG/ND/076	Cement	− 7.5	− 1.5
Poorly bedded wackestone	BG/ND/075	Cement	− 17.5	− 1.2
Poorly bedded wackestone	BG/ND/074	Matrix	− 16.1	− 1.4
Poorly bedded wackestone	BG/ND/073	Matrix	− 18.0	− 0.9
Poorly bedded wackestone	BG/ND/072	Cement	− 18.6	− 0.8

Table 1 (continued)

Facies name	Sample no	Content	$\delta^{18}O‰$ (VPDB)	$\delta^{13}C‰$ (VPDB)
Poorly bedded wackestone	BG/ND/071	Cement	− 5.2	− 0.2
Poorly bedded wackestone	BG/ND/070	Matrix	− 6.5	− 1.4
Poorly bedded wackestone	BG/ND/069	Matrix	− 6.4	− 1.4
Poorly bedded wackestone	BG/ND/068	Cement	− 4.3	− 1.4
Poorly bedded wackestone	BG/ND/067	Cement	− 10.8	− 2.7
Poorly bedded wackestone	BG/ND/066	Matrix	− 6.2	− 0.7
Poorly bedded wackestone	BG/ND/065	Matrix	− 5.6	− 1.7
Poorly bedded wackestone	BG/ND/064	Matrix	− 6.6	− 0.3
Poorly bedded wackestone	BG/ND/063	Matrix	− 5.9	− 0.3
Poorly bedded wackestone	BG/ND/062	Matrix	− 6.2	0.2
Poorly bedded wackestone	BG/ND/061	Matrix	− 6.4	0.2
Poorly bedded wackestone	BG/ND/060	Matrix	− 6.6	− 0.7
Nodular wackestone	BG/ND/059	Cement	− 7.6	− 3.1
Nodular wackestone	BG/ND/058	Matrix	− 5	2
Nodular wackestone	BG/ND/057	Cement	− 16.6	0.6
Nodular wackestone	BG/ND/056	Cement	− 9.1	0.6
Nodular wackestone	BG/ND/055	Cement	− 14.0	0.0
Nodular wackestone	BG/ND/054	Cement	− 15.3	0.7
Nodular wackestone	BG/ND/053	Cement	− 15.6	0.9
Nodular wackestone	BG/ND/052	Cement	− 15.4	0.7
Nodular wackestone	BG/ND/051	Cement	− 12.2	− 1.6
Nodular wackestone	BG/ND/050	Cement	− 17.4	0.4
Nodular wackestone	BG/ND/049	Cement	− 18.2	− 0.2
Nodular wackestone	BG/ND/048	Matrix	− 4.2	0.8
Nodular wackestone	BG/ND/047	Cement	− 6.6	− 1.2
Nodular wackestone	BG/ND/046	Cement	− 6.3	− 1.4
Nodular wackestone	BG/ND/045	Cement	− 4.8	− 0.8
Nodular wackestone	BG/ND/044	Cement	− 6.7	− 2.8
Nodular wackestone	BG/ND/043	Cement	− 6.1	− 2.1
Nodular wackestone	BG/ND/042	Cement	− 6.5	− 2.6
Nodular wackestone	BG/ND/041	Cement	− 6.2	− 2.3
Nodular wackestone	BG/ND/040	Matrix	− 6.7	0.0
Nodular wackestone	BG/ND/039	Matrix	− 7.3	− 1.0
Nodular wackestone	BG/ND/038	Matrix	− 6.2	− 0.2
Nodular wackestone	BG/ND/037	Cement	− 8.9	− 5.6
Nodular wackestone	BG/ND/036	Matrix	− 6.4	0.1
Nodular wackestone	BG/ND/035	Matrix	− 6	1.1
Nodular wackestone	BG/ND/034	Matrix	− 4.5	− 0.9
Nodular wackestone	BG/ND/033	Cement	− 6.7	− 3.7
Nodular wackestone	BG/ND/032	Matrix	− 6.3	0.1
Nodular wackestone	BG/ND/031	Cement	− 9.6	− 2.1
Nodular wackestone	BG/ND/030	Matrix	− 6.7	− 1.7
Nodular wackestone	BG/ND/029	Cement	− 4.6	2.0
Nodular wackestone	BG/ND/028	Cement	− 5.3	− 0.8
Nodular wackestone	BG/ND/027	Matrix	− 7.3	− 1.8
Nodular wackestone	BG/ND/026	Matrix	− 6.3	− 0.3
Nodular wackestone	BG/ND/025	Matrix	− 6.4	0.3
Nodular wackestone	BG/ND/024	Matrix	− 6.3	− 0.3
Nodular wackestone	BG/ND/023	Matrix	− 6.2	0.0
Nodular wackestone	BG/ND/022	Matrix	− 6.6	− 0.1
Wackestone-mudstone alternation	BG/ND/021	Cement	− 6.8	− 3.6

Table 1 (continued)

Facies name	Sample no	Content	$\delta^{18}O$‰ (VPDB)	$\delta^{13}C$‰ (VPDB)
Wackestone-mudstone alternation	BG/ND/020	Cement	− 20.2	0.5
Wackestone-mudstone alternation	BG/ND/019	Cement	− 19.6	0.7
Wackestone-mudstone alternation	BG/ND/018	Cement	− 18.8	0.2
Wackestone-mudstone alternation	BG/ND/017	Cement	− 8.1	0.8
Wackestone-mudstone alternation	BG/ND/016	Matrix	− 8.6	0.9
Wackestone-mudstone alternation	BG/ND/015	Cement	− 18.5	0.7
Wackestone-mudstone alternation	BG/ND/014	Cement	− 13.6	− 0.5
Wackestone-mudstone alternation	BG/ND/013	Cement	− 12.2	− 0.4
Wackestone-mudstone alternation	BG/ND/012	Cement	− 18.2	0.7
Wackestone-mudstone alternation	BG/ND/011	Cement	− 14.4	− 0.2
Wackestone-mudstone alternation	BG/ND/010	Matrix	− 6.5	− 0.2
Wackestone-mudstone alternation	BG/ND/009	Cement	− 6.7	− 2.7
Wackestone-mudstone alternation	BG/ND/008	Cement	− 7.0	− 2.7
Wackestone-mudstone alternation	BG/ND/007	Cement	− 8.1	− 3.3
Wackestone-mudstone alternation	BG/ND/006	Matrix	− 3.9	2.9
Wackestone-mudstone alternation	BG/ND/005	Cement	− 15.3	1.1
Wackestone-mudstone alternation	BG/ND/004	Matrix	− 6.2	0.2
Wackestone-mudstone alternation	BG/ND/003	Matrix	− 6.4	0.2
Wackestone-mudstone alternation	BG/ND/002	Matrix	− 6.0	− 0.1
Wackestone-mudstone alternation	BG/ND/001	Matrix	− 6.4	− 2.3
Wackestone-mudstone alternation	BG/ND/000	Matrix	− 6.4	− 0.8
Wackestone-mudstone alternation	BG/ND/001	Matrix	− 6.6	− 0.7
Bryozoan Limestone Formation	BG/ND/O/17	Bioclast	− 7.5	− 2.5
Bryozoan Limestone Formation	BG/ND/O/16	Bioclast	− 5.8	− 1.24
Bryozoan Limestone Formation	BG/ND/O/15	Bioclast	− 6.6	− 3.32
Bryozoan Limestone Formation	BG/ND/O/14	Bioclast	− 5.9	− 2.62
Bryozoan Limestone Formation	BG/ND/O/13	Bioclast	− 6.8	− 2.52
Bryozoan Limestone Formation	BG/ND/O/12	Bioclast	− 6.7	− 3.354
Bryozoan Limestone Formation	BG/ND/O/11	Bioclast	− 6.4	− 2.36
Bryozoan Limestone Formation	BG/ND/O/10	Bioclast	− 5.3	− 1.12
Nodular Limestone Formation	BG/ND/O/09	Bioclast	− 6.8	− 2.41
Nodular Limestone Formation	BG/ND/O/08	Bioclast	− 6.2	− 2.06
Nodular Limestone Formation	BG/ND/O/07	Bioclast	− 6.6	− 2.37
Nodular Limestone Formation	BG/ND/O/06	Bioclast	− 4.6	0.168
Nodular Limestone Formation	BG/ND/O/05	Bioclast	− 6.6	− 1.9
Nodular Limestone Formation	BG/ND/O/04	Bioclast	− 6.8	− 2.01
Nodular Limestone Formation	BG/ND/O/03	Bioclast	− 7.0	− 2.028
Nodular Limestone Formation	BG/ND/O/02	Bioclast	− 6.0	− 2.06
Nodular Limestone Formation	BG/ND/O/01	Bioclast	− 6.8	− 3.6
Nodular Limestone Formation	BG/ND/O/00	Bioclast	− 7.6	− 3.1
Nodular Limestone Formation	BG/ND/O/01	Bioclast	− 5.3	− 0.4

Nodular Limestone

The average thickness of the Nodular Limestone is around 5 m. The Nodular Limestone Formation comprises three non-repetitive facies, wackestone-mudstone alternations, nodular wackestone and poorly bedded wackestone.

Wackestone-mudstone alternation Overlying the Nimar Formation, the thickness of the wackestone-mudstone alternation varies from 1.7 to 3.1 m. The thickness of constituent beds varies from 3 to 7 cm, and color generally varies from dark gray to pinkish-gray (Fig. 3a). The beds show tabular geometry. The vertical sections of both mud-
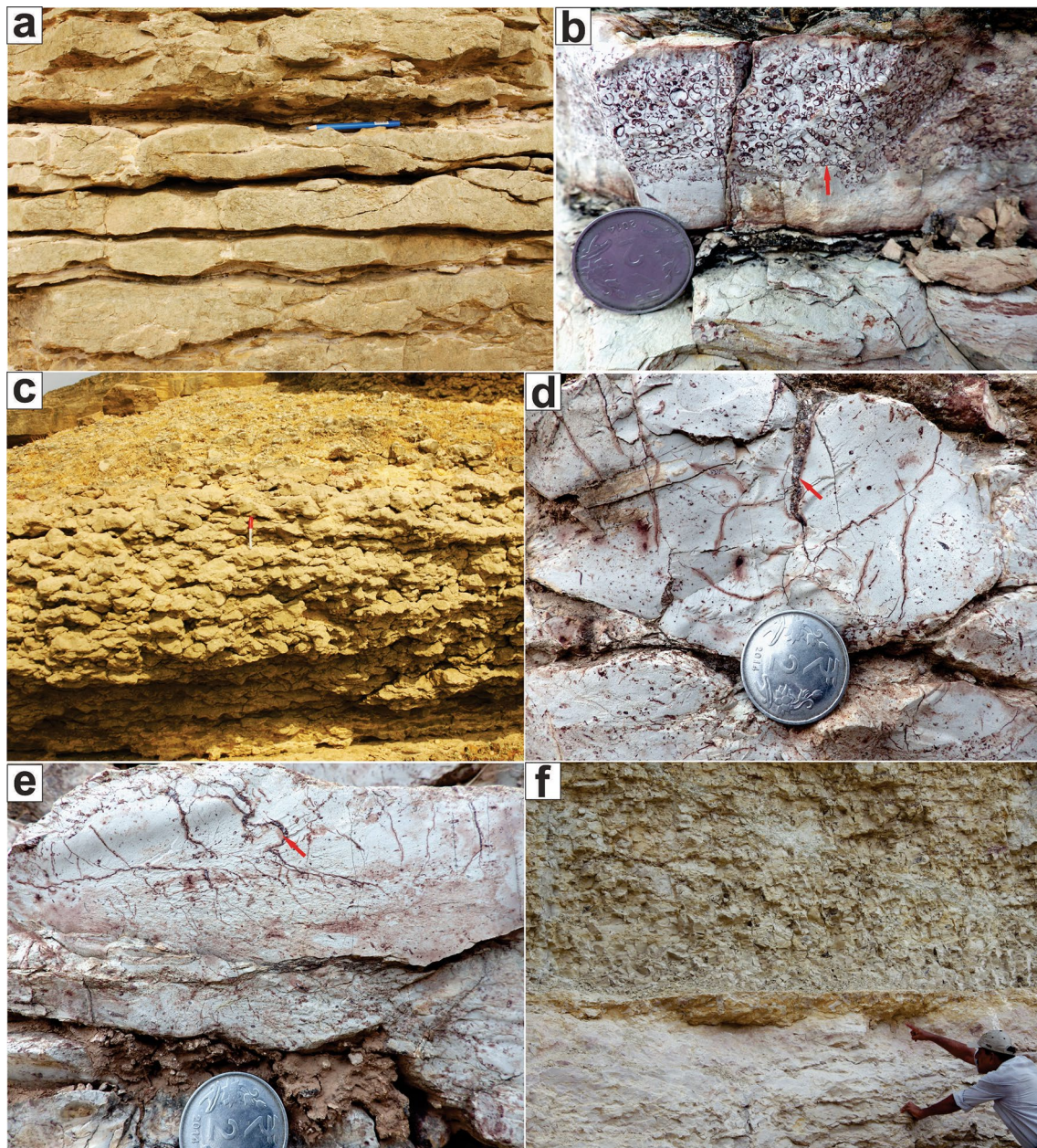
Fig. 3 Field photographs showing wackestone-mudstone alternation facies (**a**); a gastropod shell-rich bed (**b**); nodules within the nodular wackestone (**c**); desiccation cracks (arrows) in vertical section of the nodular wackestone (**d**, arrow) with root structure (**e**, arrow); poorly bedded wackestone facies (**f**) (hammer length = 38, pen length = 14 cm, coin diameter = 2.7 cm)

stones and wackestones often exhibit desiccation cracks. A gastropod-rich bed of ~ 5 cm thick occurs at the top of the facies (Fig. 3b). Although primary sedimentary structures are poorly preserved, the beds may exhibit ripple laminae in places. The wackestone contains abundant cacispheres exhibiting small circular to elliptical spar-filled structures (Fig. 4a). The calcispheres are often impregnated by Fe-oxide. The diameters of calcispheres vary from 10 to 150 µm. Most of the bioclasts are dissolved, leaving moldic pores. The voids are mostly filled by geopetal sediments.

The wackestone beds often contain peloid, pisoid, intraclast and relics of bioclasts such as gastropods, echinoderms, molluscs and forams.

The abundance of micrite, poor sorting of bioclasts as well as intact nature of bioclasts reflect a low-energy environment of deposition. The paucity of marine fossils and sparse bioturbation indicates a restricted to semi-restricted intertidal to supratidal environments (Colombié and Strasser 2005). Abundant calcispheres and rare small foraminifers in micritic groundmass corroborate a
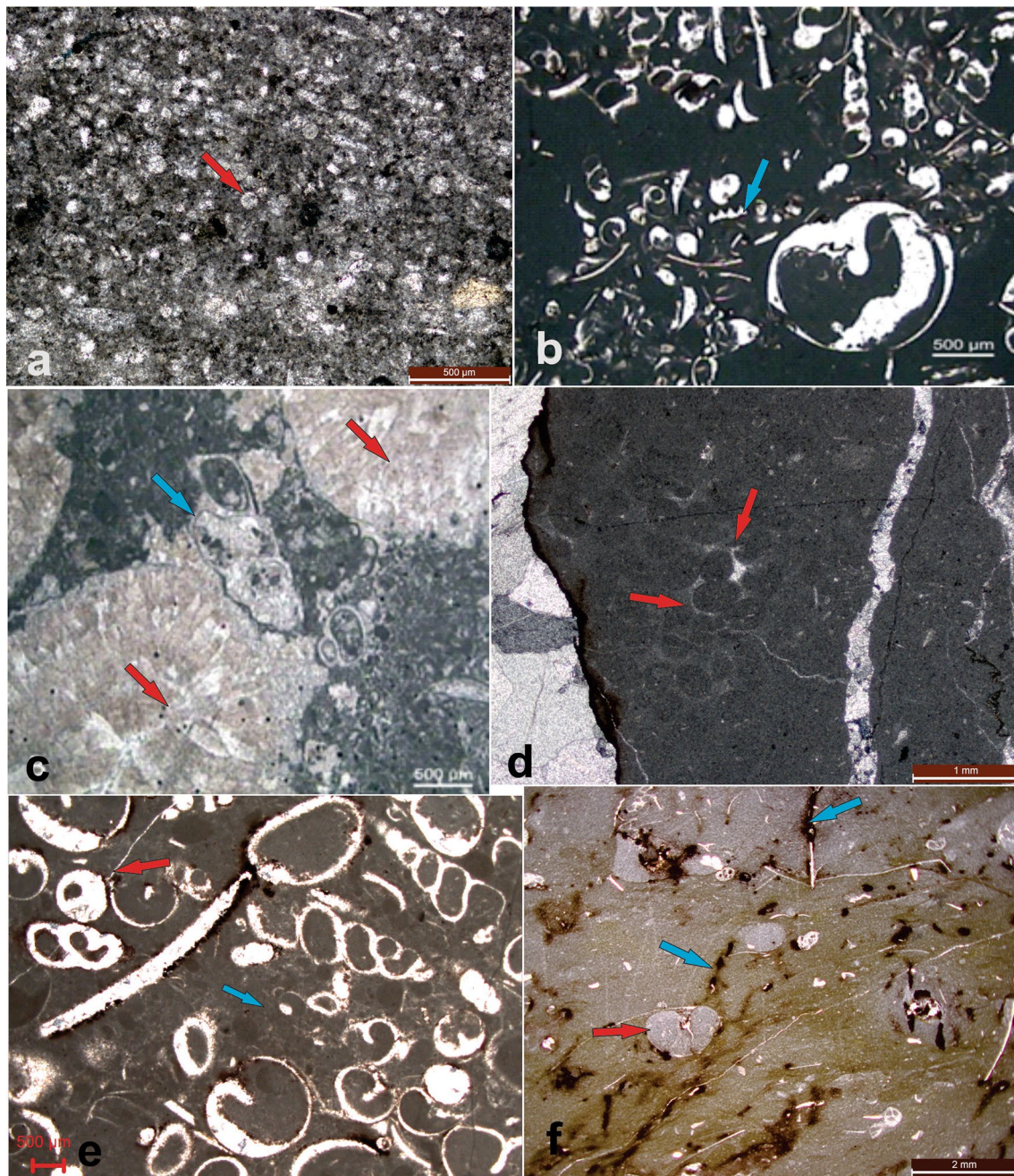
Fig. 4 Photomicrographs under plane polarized light: Thin section of wackestone-mudstonre showing intensively calichified biopelsparite consisting of peloids-pisoids, intraclasts and relics of bioclasts (arrows) (**a**); haphazardly oriented bioclasts and biomolds (**b**); thin section of nodular wackestone showing a gastropod shell (blue arrow) between nodules (red arrow) (**c**); rounded to irregular pisoids (red arrows), (**d**); thin section of poorly bedded wackestone showing gastropoda (yellow arrow) cut across by a root (red arrow), with alveolar texture (blue arrow), (**e**); hairy, wavy and bifurcated rootlets (blue arrows) with foram (red arrow) (**f**)

low-energy depositional setting (Tucker and Wright 1990; Flügel 2004; Sellwood 1993; Adabi et al. 2008; Racey et al. 2016). Overall, the facies indicate a low-energy, upper intertidal to supratidal depositional environment undergoing frequent exposures.

Nodular wackestone This facies overlies gradationally the wackestone-mudstone alternation and consists predominantly of wackestone. The average thickness of the facies varies from 1.6 to 2.9 m. The facies exhibits distinct nodularity in wackestone beds, which locally grades into pack-

stone. The nodules are primarily made up of lime mudstone. Although most nodules are broadly spherical (diameter 3–7 cm), some are ellipsoidal (Fig. 3c). The vertical sections, as well as bedding planes of the nodular laminated beds often exhibit desiccation cracks and root structures (Fig. 3d, e). These beds are often associated with thin mudstone layers showing irregularly developed, polygonally-cracked surfaces. A 20 cm-thick hardground surface occurs at the top of the nodular wackestone. Brachiopods, pelecypods, and gastropods encrust the hardground surface. It predominantly consists of micrite with abundant gastropods, echinoderms/echinoid spines, and molluscs. The bioclasts comprise both intact and broken shell fragments, which are commonly bored. Biomolds are surrounded by a thin halo of dog-tooth cement; the remaining space is filled with a mosaic of coarse-grained xenotopic cement (Fig. 4b). The main matrix is either micritic or micro-bioclastic. It is characterized by micro-nodular texture of a calichified matrix that has been sometimes cemented by radiaxial type. Small gastropod shells may occur within the matrix (Fig. 4c). Hairy and bifurcated rootlets impregnated by Fe-oxides occur in a few places. Sediments often exhibit in-situ brecciated rootlets and alveolar-septal texture of rhizoconcretions. Pisoid appears as more or less rounded grains, coated with micritic laminae (Fig. 4d). They vary in diameter from 2 to 8 mm. Pisoids appear darker than the surrounding micritic matrix and consist of irregular micrite laminae. The intergranular spaces between pisoids exhibit meniscus cement. Sheet cracks are filled with internal sediment.

The abundance of micrite, poor sorting of bioclasts, as well as good preservation state of bioclasts (echinoderms, gastropods) suggests a low-energy environment of deposition. The presence of desiccation cracks pisoids, rhizoconcretions, alveolar-septal texture, in-situ brecciation and micro-nodulation reflect long periods of subaerial exposure and pedogenesis (Calvet and Julia 1983; Flügel 2004; Pomoni-Papaioannou and Zampetakis-Lekkas 2009). The absence of primary sedimentary structures in nodular beds suggests pedogenic modification. The hardground surface, associated with borings and encrustations, and filled with silt- to sand-sized particles in a micritic to microsparitic matrix, reflects meteoric diagenesis (Zampetakis-Lekkas et al. 2007). Secondary dissolution cavities, principally biomolds filled with internal sediment (vadose silt, sensu Dunham 1969a; Dunham 1969b) and drusy/blocky cement corroborates the meteoric diagenetic modification of the original lime mudstone (Pomoni-Papaioannou and Zampetakis-Lekkas 2009; Pomoni-Papaioannou and Karakitsios 2016). Thus, the sediment surface was lithified rapidly, and colonized by boring and encrusting endofauna and epifauna, following the marine incursion.

Poorly bedded wackestone Resting on a hardground surface, the topmost facies of the Nodular Limestone Formation consists of poorly bedded wackestones. The beds appear either crudely laminated or massive. Bioclasts are less abundant than those in the nodular wackestone. The thickness of this facies varies from 1.3 to 2.4 m (Fig. 3f). Root traces are often found in-situ. Vertical and horizontal burrows may occur in places. A 20 cm-thick iron-stained hardground develops at the top of the facies, which separate the Nodular Limestone below and the Bryozoan Limestone above. The top part of the Nodular Limestone Formation often contains a few broken fragments of bryozoan.

Petrographic examination reveals alveolar texture and intensive calichification. Rhizoids, which are red spots of Fe-oxides dispersed in the matrix, display alveolar texture and hairy, wavy and bifurcated rootlets (Fig. 4e, f). Pisoids are more or less rounded grains, coated with irregular micritic laminae. The coatings are made up of irregular, dark micrite laminae alternating with lighter micrite layers that may include small pisoids. Bioclasts, mainly gastropod, bivalve and rare foraminifera, occur in patches and are frequently impregnated by Fe-oxides. Bioclasts are often dissolved and their molds are filled with blocky calcite cement. Coarse crystalline spar occurs within the breccia. In some places, hairy desiccation cracks are found (Fig. 4f). The micrite is recrystallized in many places to form microspars. Some anastomosing recrystallized non-fabric selective veins are present with a medium-grained sparry fabric. In some places, micrite appears like vadose silt. The nodules are small and appear darker than the surrounding matrix. Bioclasts are dissolved and partially filled with micrite within the hardground. Some vadose silt may occur within the hardground. Broken fragments of bioclasts such as brachiopods, pelecypods, gastropods and rare foraminifera fill the borings. The abundance of lime mudstone indicates a low-energy environment of deposition (Tucker and Wright 1990; Spence and Tucker 1997; Wilson and Evans 2002; Flügel 2004; Fournier et al. 2004; Rasser et al. 2005; Banerjee et al. 2018). The subaerial exposure condition is evident by the brecciation, root-traces, pisoids, desiccation and recrystallization (Flügel 2004). The brecciation and recrystallization processes tend to be more active in the upper part of the soil horizon. The facies, therefore, indicates pedogenesis during long periods of subaerial exposure (Strasser 1991; Wright 1994; Sattler et al. 2005; Zampetakis-Lekkas et al. 2007; Pomoni-Papaioannou and Zampetakis-Lekkas 2009; Pomoni-Papaioannou and Karakitsios 2016). The deposition possibly took place in an upper intertidal to supratidal environment with profound development of paleosol (Martin-Chivelet and Giménez 1992; Gómez-Gras and Alonso-Zarza 2003).

Facies of the Bryozoan Limestone Formation

The overlying Bryozoan Limestone Formation begins with a cross-stratified rudstone consisting predominantly of broken shells of bryozoans, bivalves, gastropods, brachiopods and echinoids. The Bryozoan Limestone Formation (also known as Coralline Limestone, Barwah Bryozoan Limestone and Chirakhan Limestone) forms low ridges in the study area, sharply overlying the Nodular Limestone Formation. Although the Formation is usually overlain by the fluvio-marine siliciclastic Lameta Formation, in many places, it is capped by the Deccan trap volcanics. The Bryozoan Limestone Formation consists of three facies, viz. cross-stratified rudstone, planar laminated rudstone and faintly laminated packstone. The planar laminated rudstone at the top is glauconitic, with abundant clastics, including quartz, feldspars and mud fragments. Facies constituting the Bryozoan Limestone Formation are described as follows.

Cross-stratified rudstone The cross-stratified fossiliferous rudstone facies rests on a hardground surface. It is well exposed around Karondia, Zeerabad, Baria, Chakrod, Kosdana, Rampura, Ratilatai and Mohi. The maximum thickness of the facies is ~ 3 m around Karondia. It consists of reddish-brown to whitish brown, thick- to thin-bedded rudstones and exhibits large-scale trough and planar cross-stratification (foreset thickness 1.1–1.5 m) passing upward to small-scale cross-stratification (foreset thickness between 10 and 20 cm). Current ripples may occur on top of the cross-stratified beds (Fig. 5a). Cross-strata show weakly bipolar flood-tide dominated paleocurrent pattern. The facies exhibits broken fragments of bryozoa besides echinoid, brachiopods, bivalve and gastropods. The rudstone is occasionally bioturbated by *Thalassinoides*. A 5–18 cm-thick, well-sorted, brachiopod-rich, dark gray to greenish-gray bed occurs at the base of the rudstone (Fig. 5b). Brachiopods are randomly distributed consisting of in-situ assemblages and also reworked forms that are highly Fe-oxide impregnated. The rudstone primarily consists of broken fragments of bryozoa (~ 80%), with a few pieces of echinoderm and echinoid spines, gastropods, brachiopods and mollusks (Fig. 6a). Fragments of coral, ostracod and foraminifera may occur locally. The length of bioclasts mostly ranges from 1 to 3 mm. Over-sized, 4–9 mm long bioclasts of echinoderms and brachiopods may occur locally. Most bioclasts, except brachiopod, are dissolved and are strongly impregnated by Fe-oxides (Fig. 5a). Dissolution and micritic coatings obscure the internal structures of bioclasts. Syntaxial overgrowth rims occur on most echinodermal grains. In places, siliciclastic grains are common and allochems are cemented by drusy calcite, enlarging towards the center of the cavities (Fig. 6b). Primary pore filling spar occurs within the chambers of foraminifera. Blocky neomorphic cement with micrite inclusions also occurs (Fig. 6b). Micrite may appear similar to vadose silt (geopetal structure), and alveolar texture and thin rhizoliths are abundant in some intervals.

Good sorting of limestone, absence of micrite, and abundant current structures indicate a high-energy depositional environment. The shape and scale of the cross-stratification indicate the migration of bedforms by current actions. The thinning-up cross-strata, coarse-grained nature of sediments and bipolarity of current structures suggest deposition in tidal channels. The dense packing of shells indicates high-energy depositional condition. Most bioclasts in this facies are characteristic of the lower intertidal environment (Gangopadhyay and Halder 1996; Gangopadhyay and Bardhan 2000; Jaitly and Ajane 2013). The meso- and micro-scale features of the facies indicates deposition in intertidal channels (cf. Calvet and Julia 1983; Pomoni-Papaioannou and Kostopoulou 2008; Pomoni-Papaioannou and Zampetakis-Lekkas 2009). Intense secondary micritization of sediments indicates prolonged calichification.

Planar laminated rudstone The planar laminated rudstone occurs below and above the faintly laminated rudstone, and is well exposed around Karondia, Ratitalai and Kosdana (Fig. 1). The topmost planar laminated rudstone appears greenish-gray because of the occurrence of glauconite (Fig. 5c). The thickness of the facies varies from 20 cm to 1.3 m. An oyster-rich bed, up to 1.1 m-thick, occurs locally at the top of the facies around Chakrod, Rotitalai, Kosdana, Baria and Karondia (Fig. 5d). Microscopic observation reveals abundant skeletal grains within the rudstone, including fragments of echinoderms, and echinoid spines, bryozoans, gastropods, ostracods, brachiopods mollusks, and foraminifera. The lengths of bioclasts vary in length from 0.5 to 2.5 mm. Most bioclasts are dissolved and coated by Fe-oxides and are strongly bored. Borings are filled with micrite and also exhibits strong micritization (Fig. 6c). The rudstone contains a moderate amount of feldspar and quartz. The content of glauconite grains varies from 10 to ~ 25%. Glauconite occurs predominantly as infillings within zooecial aperture of bryozoa (Fig. 6d) and rarely within pore spaces of echinoid spines and carapace of ostracoda. The average diameter of individual bryozoan infilling varies from 40 μm to 250 μm. Petrographic examination reveals frequent replacement of K-feldspar by glauconite.

The rudstone containing abundant clastics, including quartz, feldspar and lime mud rock fragments indicates supply of siliciclastics in adjacent coastal regions. Planar lamination indicates a high-energy depositional condition. The oyster bed at the top further suggests lower intertidal depositional setting. The presence of glauconite reflects stratigraphic condensation at the top of the Bryozoan Limestone Formation (Banerjee et al. 2016a). Recently Bansal et al. (2019) presented a detailed investigation on the formation
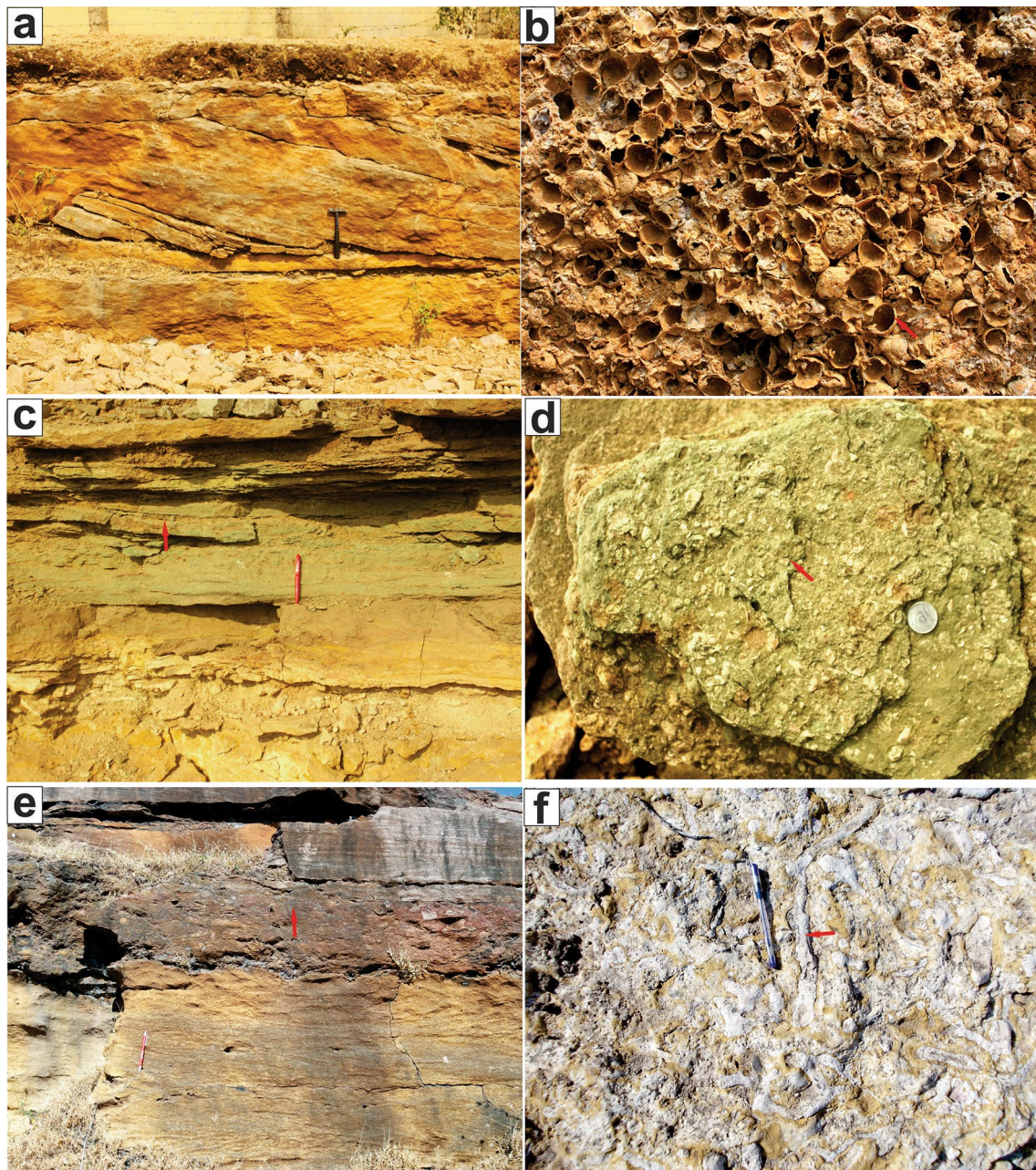
Fig. 5 Field photograph showing a vertical section of the cross-stratified rudstone (**a**) vertical section of a brachiopod-rich bed in outcrop (**b**); vertical section of glauconite-bearing planar laminated rudstone (**c**) bedding plane of oyster-rich bed at the top of the faintly laminated packstone (**d**); faintly laminated packstone showing sandwich between two bed (**e**); Thalassinoides on a bedding surface (**f**); (pen length in **a**, **b**, **c** = 14 cm; hammer length in **a** = 38 cm, coin diameter in **d** = 2.7 cm; width of outcrop in b = 23 cm)

of the glauconitic bed within the Bryozoan Limestone and concluded that similar shallow marine glauconite formed along the paleo-Tethyan belt, which is related to the Turonian eustatic sea level rise.

Faintly laminated packstone This facies consists of poorly bioturbated fossiliferous packstone, sandwiched between two planar laminated rudstones (Fig. 5e). The thickness of

the facies ranges from 1 m to 1.5 m. It locally crops out at Kosdana, Baria and Karondia. Thalassinoides may be found occasionally, with burrow diameter ranging from 1 to 2.5 cm (Fig. 5f). Body fossils include entire brachiopod shell and skeletal fragments. The facies is dominated by bioclastic packstones exhibiting grain-supported fabric, with well-sorted allochems (Fig. 6e). Bioclasts, including bryozoan, echinoderm, and bivalve comprise up to 80% of
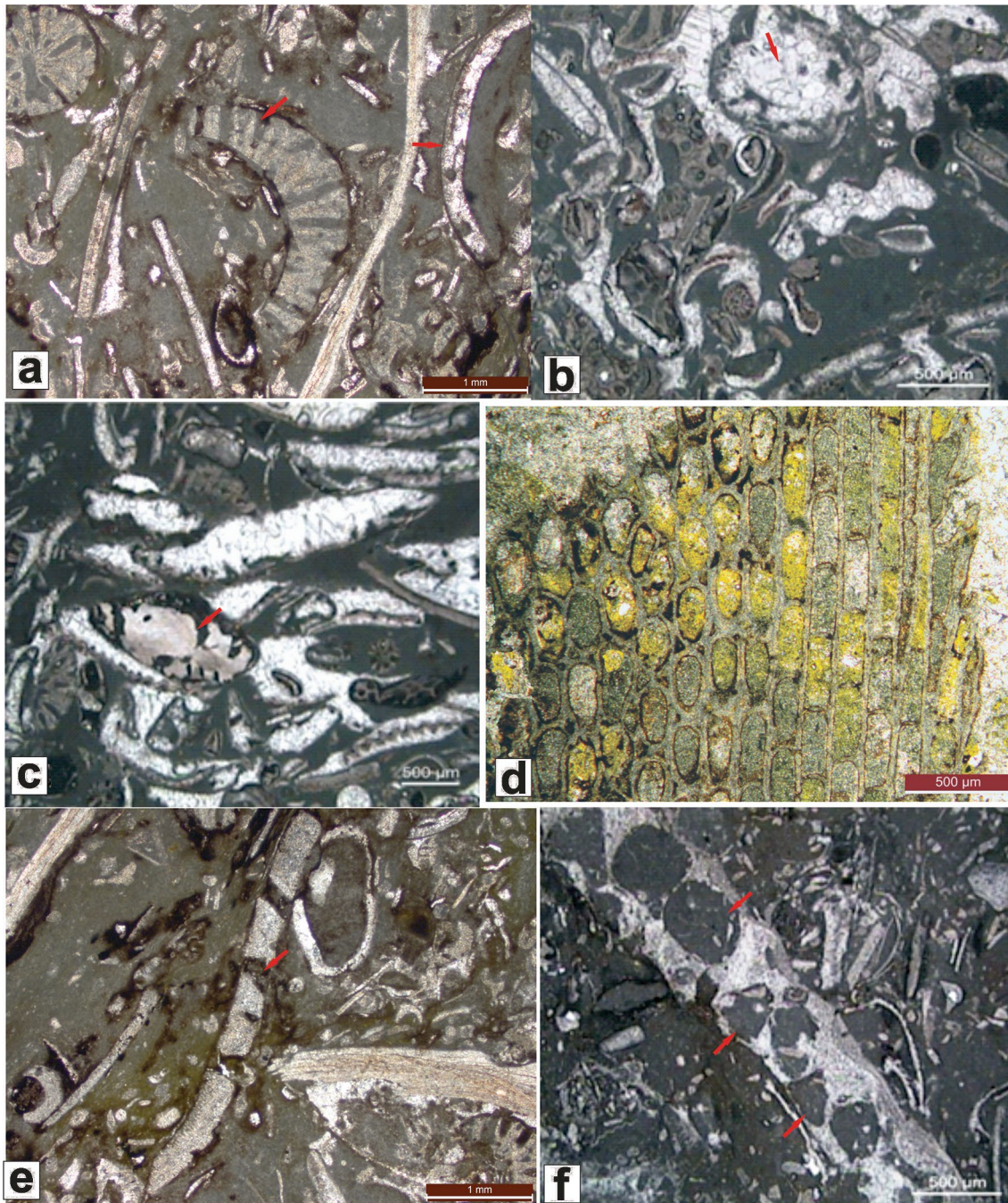
Fig. 6 Photomicrographs of thin sections of cross-stratified rudstone under cross polars showing micritic coatings around bioclasts (red arrows) (**a**); Photomicrographs under plane polarized light: enlarged dissolution cavities (red arrow) (**b**); Allochems cemented by drusy spars (**c**); glauconite within zooids in planar laminated rudstone (**d**); micritized bioclasts in faintly laminated packstone marked by arrow (**e**) and borings in echinoderm filled by micrite (red arrow) (**f**)

the rock. Most bioclasts are dissolved and filled with calcite spars. Shell fragments are either partly micritized or recrystallized (Fig. 6e, f). Secondary porosity is filled with micrite within shell cavities.

The bioturbated packstone facies represents moderate-energy depositional conditions. Petrographic and biotic attributes of the facies relate it to lower intertidal deposits (cf. Pomoni-Papaioannou and Zampetakis-Lekkas 2009). *Thalassinoides* burrows suggest near-shore environments with moderately high energy conditions (Singh et al. 1983). Abundant meniscus cement and biomolds further

support meteoric vadose diagenetic modification (cf. Pomoni-Papaioannou and Zampetakis-Lekkas 2009).

Paleogeography and depositional sequence of the Bagh carbonates

Overlying the Nimar Formation the Bryozoan Limestone indicates the continuation of the marine transgression and curtailment of siliciclastics. The dominance of lime mudstone in facies constituting the Nodular Limestone Formation indicates a low-energy environment of deposition (Fig. 7). The Nodular Limestone Formation exhibits well-developed calichification due to long-lasting subaerial exposure. Nodule formation is attributed to pedogenic modification driven by root activities. Abundant pedogenic features including root-related structures (rhizoliths), vadose silt (geopetal texture) and pisoids indicate subaerial exposure of the depositional substrate (James and Choquette 1990; Wright 1994; Kraus and Hasiotis 2006). The paucity of marine fossils and sparse bioturbation corroborate deposition in supratidal and upper intertidal settings (Colombié and Strasser 2005; Pomoni-Papaioannou and Karakitsios 2016). The environmental interpretation agrees well with the paleontological data of the Nodular Limestone Formation (cf. Gangopadhyay and Halder 1996; Akhtar and Khan 1997; Gangopadhyay and Bardhan 2000).

The Bryozoan Limestone Formation, beginning with a cross-stratified rudstone, suggests an increase in energy condition. Tide-originated sedimentary features like reactivation surface and weak bipolarity in cross-stratification orientation indicate deposition in flood-tide dominated shallow channels in the lower intertidal environment (Fig. 7). Occasional exposure of the sediments causes intense calichification, in-situ brecciation, rhizoliths, alveolar-septal texture and circumgranular cracks. The study of the constituent facies suggests a lower intertidal depositional condition (cf. Pomoni-Papaioannou and Kostopoulou 2008; Pomoni-Papaioannou and Zampetakis-Lekkas 2009). The planar laminated rudstone, containing abundant quartz and feldspar grains corroborates the shallowing of the depositional environment.

The Nimar Formation, consisting primarily of shallow marine sandstones exhibits a transgressive trend (Bose and Das 1986; Bhattacharya and Jha 2014). The transgressive trend continues within the Nodular Limestone and the overlying Bryozoan Limestone (Fig. 8). The deposition of the Nodular Limestone takes place in supratidal and upper intertidal environments undergoing repeated subaerial exposure. The cross-stratified rudstone facies of the Bryozoan Limestone Formation represents channel deposits within the lower intertidal environment. Subaerial exposure surfaces within the Nodular Limestone and Bryozoan Limestone bear
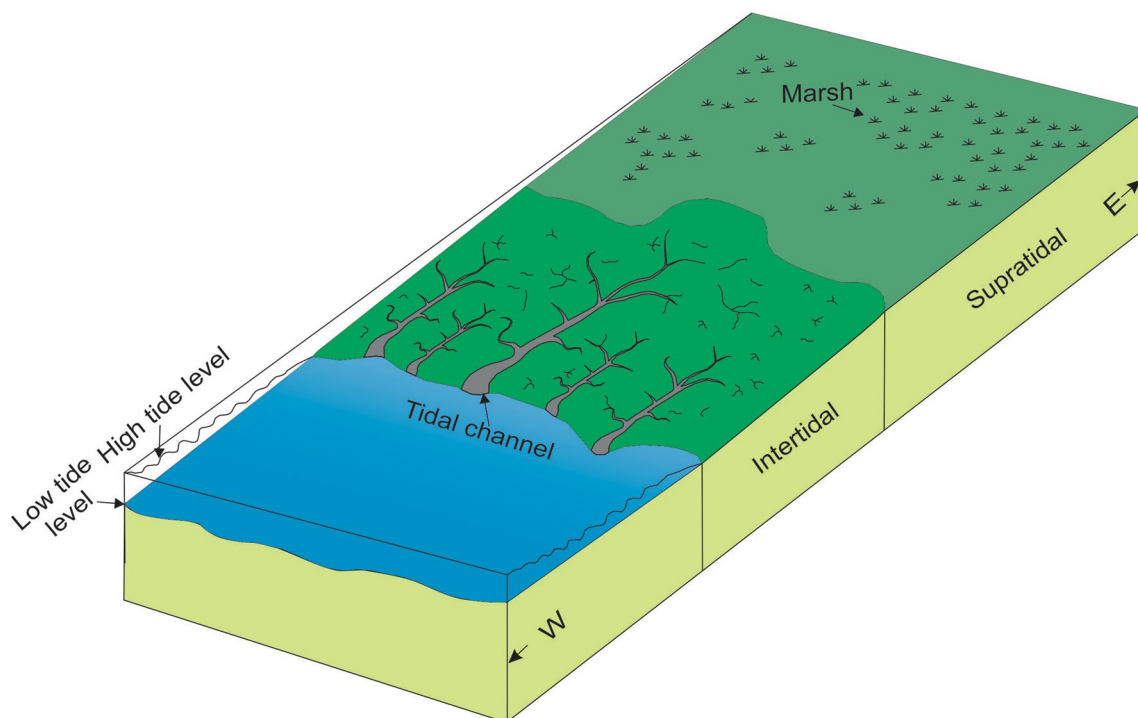

Fig. 7 Depositional model showing spatial distribution of constituent facies of the Nodular Limestone and the Bryozoan Limestone. While the Nodular Limestone was deposited in low-energy supratidal to upper intertidal environment, the deposition of Bryozoan Limestone took place in lower intertidal environment including tidal channels
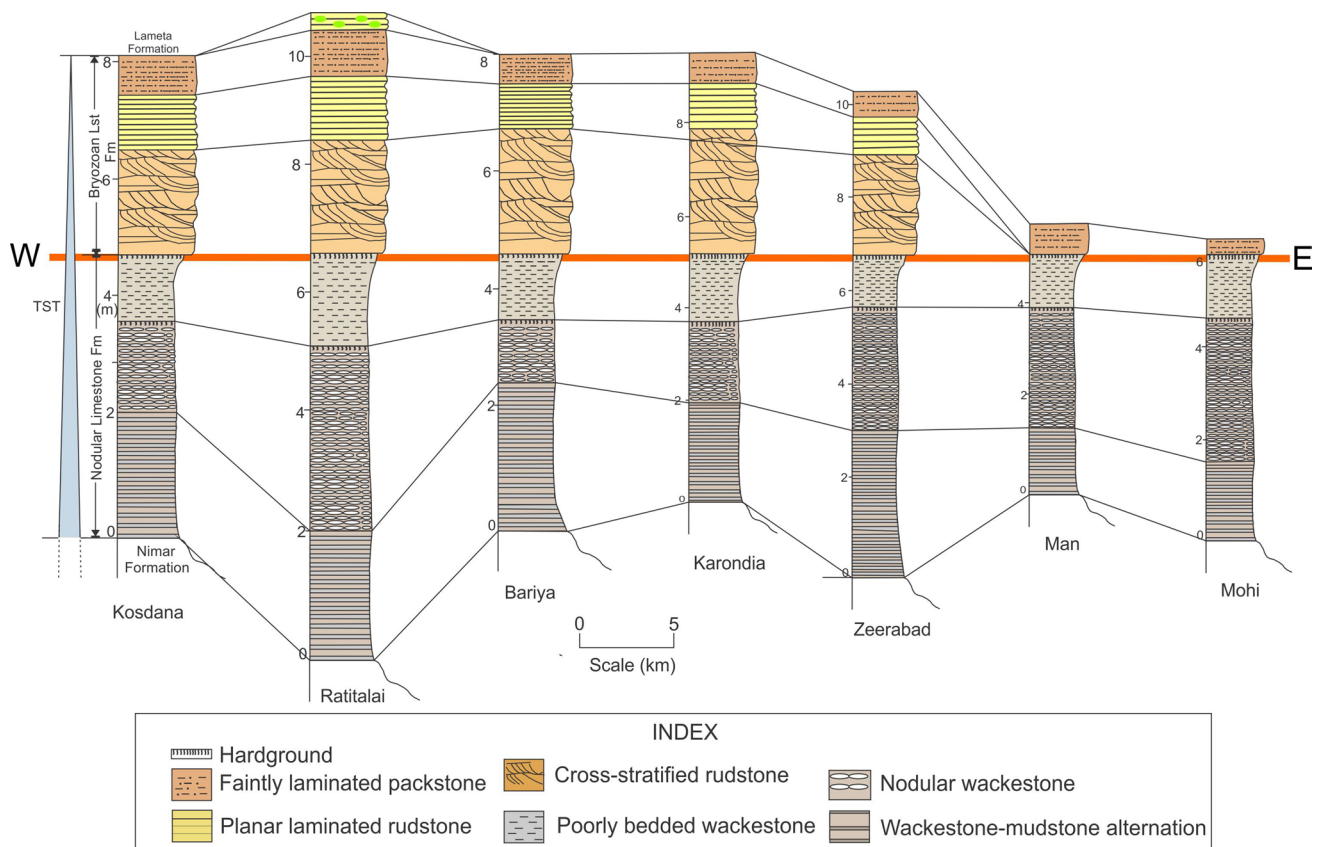
Fig. 8 Panel showing lateral correlation of Nodular Limestone and Bryozoan Limestone across different sections

subtle evidence of significant breaks in sedimentation. The glauconite bed within the Bryozoan Limestone represents the boundary between the overall transgressive Bagh Group and the prograding Lameta Formation (Fig. 8). Thicknesses of the constituent facies broadly increase towards the open ocean. A stratigraphic condensation near the top of the transgressive systems and the input of clastic supply has allowed the formation of glauconite (Banerjee et al. 2016a, b; Bansal et al. 2019).

Diagenetic evolution of carbonates in Bagh Group

Luminescence characteristics

The most important diagenetic processes affecting the Bagh Group of carbonates are cementation, micritization, neomorphism, minor compaction and fracturing. Thin sections of selected samples were investigated for their luminescence patterns. These carbonates exhibit broadly five luminescence types for bioclasts, micrite and three different spars viz. C1, C2 and C3 (Fig. 9a–f). Isotope ratios of all five varieties of carbonates are presented in Figs. 10 and 11.

Bioclast: identified on the basis of primary fabric, mostly non-luminescent, bryozoan and oyster shells are found most unaltered

Micrite or microspar (M): tiny, non-luminescent to weakly luminescent

C1 spar: acicular shape, tiny, non-luminescent to weakly luminescent, immediately overlying grains

C2 spar: blocky morphology with drusy fabric, bright luminescence

C3 spar: blocky morphology with drusy fabric, non-luminescent to dark, often showing bright to dull zonation.

Morphology, as well as the luminescence pattern, indicates marine, meteoric and burial origin for C1, C2 and C3 spars, respectively (cf. Machel et al. 1991; Machel 2000; Major 1991; Boggs and Krinsley 2006; Brand et al. 2012; Sarkar et al. 2014). Morphology of cements and their luminescence characteristics reveal that the marine-originated C1 spar was succeeded by the meteoric cementation (C2 spar). This was followed by the pedogenesis, and finally, cementation took place in burial condition (C3 spar).
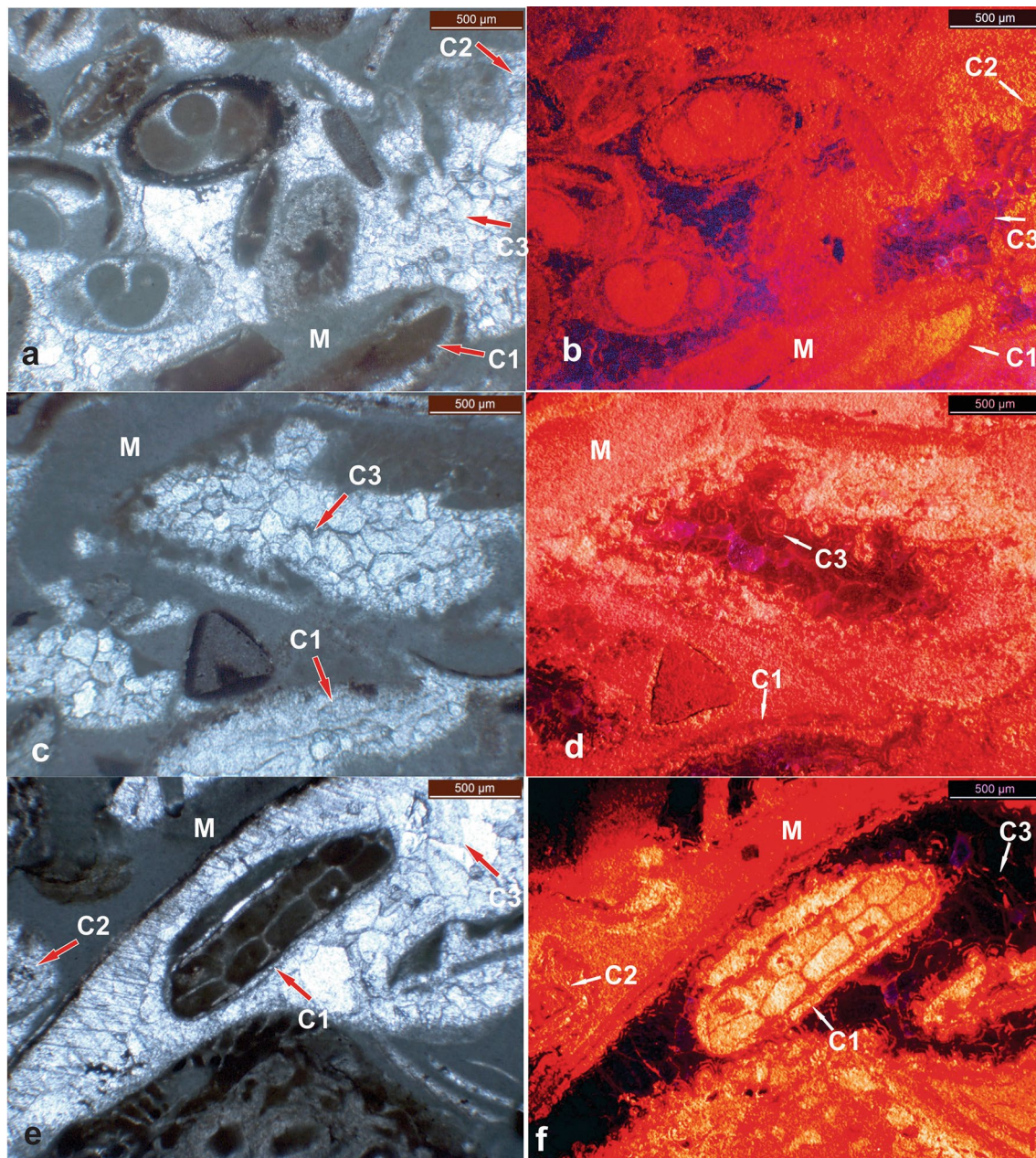
Fig. 9 Photomicrographs under plane polarized light (**a**, **c**, **d**) and corresponding cathodoluminescence images (**b**, **d**, **f**), showing the same field of view (B-bioclast, M-micrite/microspar; C1-marine cement; C2-meteoric cement; C3-burial cement (detailed description in text)

Isotopic ratios of Bagh carbonates

Carbon and oxygen isotopic ratios of carbonate samples were determined separately for micrite/microspar, bioclasts (bryozoa and oyster) C1, C2 and C3 spars using the Micro-Mill facility. Isotope ratios are provided in Table 1.

Isotope ratios of the Nodular Limestone Formation The $\delta^{13}C$ ratios of micrite to microspar and oyster and bryozoan shell samples of the Nodular Limestone Formation

range from $-2.3‰$ to $+2.9‰$. Around 90% of data plot between $-2‰$ and $+2‰$. The $\delta^{18}O$ ratios of micrite to microspar, as well as oyster and bryozoa samples of the Nodular Limestone mostly range between $-3‰$ and $-7‰$. The $\delta^{18}O$ values of samples of poorly bedded wackestone appear most consistent, ranging between $-5.6‰$ and $-6.6‰$ (av. $-6.6‰$). The $\delta^{13}C$ and $\delta^{18}O$ ratios of micrite/microspar samples of the Nodular Limestone Formation exhibit poor correlation ($r^2 = 0.3$; $p = 0.03$; Fig. 10a). A cross plot between $\delta^{13}C$ and $\delta^{18}O$ ratios distinguishes three varieties

Fig. 10 Cross-plot between δ¹⁸O and δ¹³C different facies of micrite/microspar and bioclast in the Nodular Limestone Formation (**a**) and different cements (**b**). Fields of average marine limestone (1), fresh water limestone (2) and meteoric cements (3) are adapted from Hudson (1977). The straight line indicates burial diagenetic trend (adapted from Choquette and James, 1987)
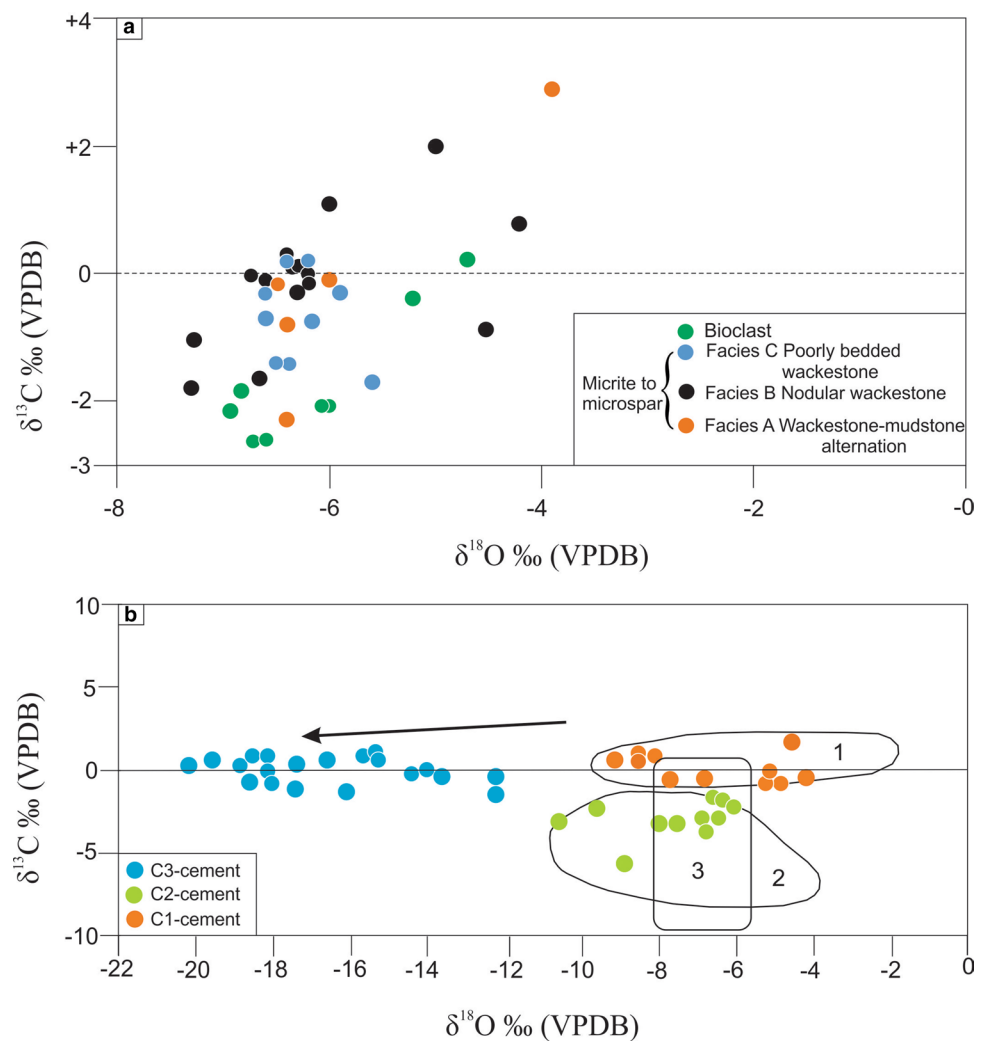
of cements based on separate clusters of data (Fig. 10b). The δ¹³C and δ¹⁸O ratios of C1 cement range from 0.9‰ to −0.8‰ and from −4.8‰ to −9.1‰ respectively. The δ¹³C and δ¹⁸O ratios for the C2 cement range from 2.0‰ to −5.6‰ and from −4.3‰ to −10.8‰ respectively. The δ¹³C and δ¹⁸O ratios for the burial-originated C3 cement range from 1.1‰ to −1.6‰ and from −12.2‰ to −20.2‰ respectively.

Isotope ratios of the Bryozoan Limestone Formation The δ¹³C ratios of micrite/microspar samples as well as oyster and bryozoan shells of the Bryozoan Limestone Formation range from −1.1‰ to −4.0‰. The δ¹³C ratios of samples of different facies overlap partially. The δ¹⁸O ratios of samples of the Bryozoan Limestone range from −5.3‰ to −9.2‰. The δ¹⁸O and δ¹³C ratios reveal a moderate correlation between δ¹⁸O and δ¹³C ($r^2 = 0.6$, $p = 0.01$) (Fig. 11a). The δ¹³C and δ¹⁸O ratios for C1 cement range from 0.2‰ to −1.5‰ and from −1.5‰ to −4.4‰ respectively (Fig. 11b). The δ¹³C and δ¹⁸O ratios for the C2 cement range from −0.9‰

to −3.72‰ and −5.8‰ to −10.2‰ respectively. While the δ¹³C and δ¹⁸O ratios for the C3 cement range from −1.0‰ to −3.0‰ and −9.5‰ to −18‰ respectively.

Diagenetic implications of isotope ratios of Bagh carbonates

The δ¹³C ratios of marine carbonate sediments remain close to 0‰, whereas carbonates precipitating from freshwater exhibit variably depleted ratios (Hudson 1977; Tucker and Wright 1990; Moore 2001; Bowen and Wilkinson 2002; Banerjee et al. 2006; Blanchet et al. 2012; Henderson et al. 2018; Scorrer et al. 2019 and many others). The diagenetic alteration tends to decrease both δ¹³C and δ¹⁸O ratios of marine carbonates (Gilleaudeau et al. 2018 and references therein). Petrographic investigation and the relationship between δ¹³C‰ and δ¹⁸O‰ ratios provide an estimation of the diagenetic resetting (Hudson 1977; Burdett et al. 1990; Banner and Hanson 1990; Joachimski 1994; Armstrong-Altrin et al. 2009; Gilleaudeau et al. 2018). The δ¹³C ratios

Fig. 11 Cross-plot between $\delta^{18}O$ and $\delta^{13}C$ different facies of micrite/microspar and bioclast in the Bryozoan Limestone Formation (**a**) and different cements (**b**). Fields of average marine limestone (1), fresh water limestone (2) and meteoric cements (3) are adapted from Hudson (1977). The straight line indicates burial diagenetic trend (adapted from Choquette and James, 1987)
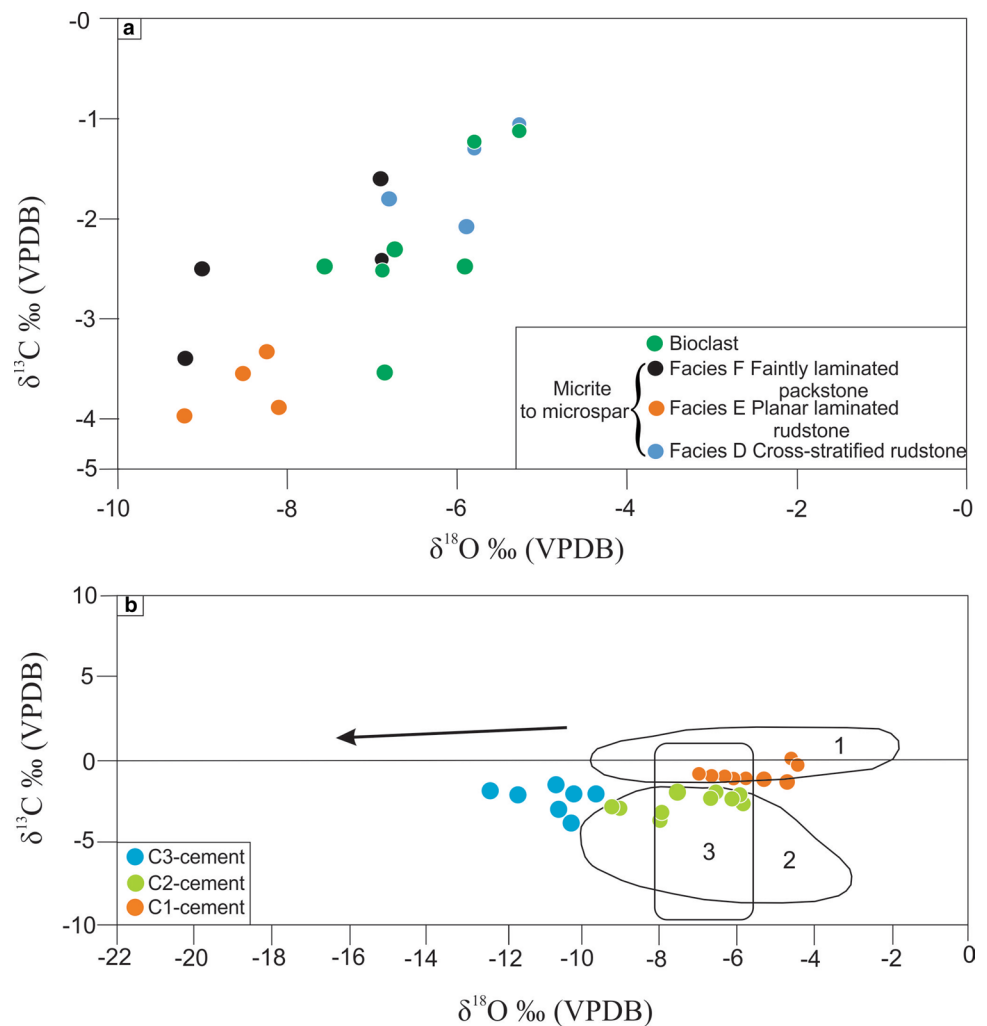
of carbonates may remain near primary at a low water/rock interaction ratio (Hudson 1977; Banner and Hanson 1990; Magaritz et al. 1991; Gilleaudeau et al. 2018). The Upper Cretaceous marine carbonate has typical $\delta^{13}C$ ratios between 1 to 3 ‰ (Wendler 2013; Jarvis et al. 2015). The $\delta^{18}O$ ratios are usually less than $-4‰$ for the Upper Cretaceous pelagic carbonates (Jarvis et al. 2015). However, the $\delta^{18}O$ ratios are sensitive to latitude and climate. Isotope ratios of cement in the Nodular Limestone and Bryozoan Limestone formations are compared with those of Hudson (1977) to recognize the extent of diagenetic alteration (Figs.10 and 11). Isotope ratios of Bagh carbonates provide the following information regarding the diagenesis of carbonates.

(a) The $\delta^{13}C$ ratios of none of the micrite/microspar samples of the Bryozoan Limestone Formation plot within the range of Late Cretaceous carbonates (cf. Wendler 2013; Jarvis et al. 2015). On the contrary, many of the micrite/microspar samples of the Nodular Limestone Formation bear the original isotopic signatures of the Late Cretaceous Ocean.

(b) Isotope ratios of C1 spars in both Nodular Limestone and Bryozoan Limestone broadly overlap with those of micrite/microspar. All data plot within the domain of the average marine limestone of Hudson (1977) (Figs. 10b and 11b). However, C1 cement in the Bryozoan Limestone Formation exhibits depleted $\delta^{13}C$ ratios compared to those of the Nodular Limestone Formation.

(c) C2 spars in both Nodular Limestone and Bryozoan Limestone are characterized by depleted $\delta^{13}C$ and $\delta^{18}O$ ratios and bright luminescence. The data points of $\delta^{13}C$ and $\delta^{18}O$ ratios plot within the fields of meteoric diagenetic cement and freshwater limestone of Hudson (1977), reflecting the diagenetic resetting of both oxygen and carbon isotopes. Petrographic evidence like calichification, in-situ brecciation, rhizoconcretions, pisoids, alveolar-septal texture, and circumgranular

cracks establish the soil formation beyond doubt in both Nodular Limestone Bryozoan Limestone.

(d) C3 spars in the Nodular Limestone Formation is characterized by highly depleted $\delta^{18}O$ ratios, varying from $-10‰$ to $-18‰$ and weakly luminescing cement (Fig. 9b). Both meteoric and burial fluids can impart $\delta^{18}O$ values between -15 and $-10‰$ on diagenetic carbonate (e.g., Derry 2010; Gilleaudeau et al. 2018). However, C3 cement is depleted in $\delta^{18}O$ ratios, with nearly unaltered $\delta^{13}C$ ratios. The isotopic signature, as well as luminescence characteristics of cements indicates burial diagenetic resetting (Fig. 9b). The comparison of isotope ratios with those of Choquette and James (1987) corroborates this interpretation. Therefore, C3 spars in both Nodular Limestone and Bryozoan Limestone, indicate shallow burial diagenetic cement.

Discussion

Although previous workers inferred the shallow marine origin for the Bagh carbonates, the facies study remained completely ignored and exposure surfaces within the succession remained unnoticed. Bagh carbonates were investigated for stable isotope ratios (cf. Bhattacharya et al. 1997). However, the meteoric diagenetic alteration of the original marine signature was overlooked. The present investigation confirms the deposition of Bagh carbonates within a shallow marine environment undergoing periodic exposures. The Nodular Limestone Formation, exhibiting well developed pedogenic and vadose diagenetic features, including geopetal, vadose pisoids, and rhizoconcretions, represents upper intertidal to supratidal deposits (Fig. 7). While the Bryozoan Limestone Formation exhibits abundant current structures and consists of coarse bioclasts, implying a moderately high-energy, lower intertidal depositional setting. The presence of reactivation surfaces, as well as weakly bipolar paleocurrent pattern, indicate the deposition of the cross-stratified rudstone in flood-dominated tidal channels (Fig. 7). Periodic exposure of the sediments causes intense calichification, cavities filled with coarse-grained drusy and poikilotopic cement, in-situ brecciation, rhizoconcretions, alveolar-septal texture, and circumgranular cracks. Overall facies character reveals a lower intertidal depositional condition.

The $\delta^{13}C$ and $\delta^{18}O$ ratios of Cretaceous shallow marine carbonates are mostly discontinuous (Heba et al. 2009). Besides, the isotope data bears the combined influence of several factors, including depositional setting, diagenetic resetting and paleosalinity (Vincent et al. 2006; Heba et al. 2009). The $\delta^{13}C$ and $\delta^{18}O$ ratios and luminescence patterns of Bagh carbonates corroborate the periodic subaerial exposure and extensive meteoric diagenetic resetting of the shallow marine carbonate deposits. Although pervasive

diagenetic resetting has obscured the original $\delta^{13}C$ and $\delta^{18}O$ ratios of micritic carbonates and C1 spars retain the least altered signatures.

Epeiric platforms do not have any modern analog. The interpretation of the facies sequence of the Late Cretaceous Bagh Group provides snapshots for ancient epicontinental platforms. The carbonate platform develops during the Cretaceous by the inundation of large parts of the continents in response to worldwide sea level highstand. The Upper Cretaceous carbonate deposits of Bagh beds, is comparable to Turonian-Coniacian marine transgressive records in Bireno and Douleb members in Zebels Barda (Jaballah and Negra 2016) and central and southern atlas of Tunisia (Camoin 1993). Platform carbonates of Mesozoic constitute important archives of past environmental change (Föllmi and Godet 2013). These deposits are influenced by processes operating at a local, regional and global scale, which are often difficult to distinguish. However, a multi-proxy approach involving thorough analysis of sedimentary sequences and investigation of samples for calcium isotopes, magnesium isotopes and ion microprobes is likely to disentangle more information regarding environmental implications of Cretaceous platform carbonates.

Conclusion

The study of the carbonate sequence of the Bagh Group leads to the following conclusions.

(a) Facies study indicates shallow marine deposition of the Bagh Group of carbonates, which underwent frequent exposure. While the Nodular Limestone Formation represents deposits within the upper intertidal to supratidal depositional settings, the Bryozoan Limestone relates to deposition in the lower intertidal setting.

(b) Petrographic evidence like calichification, in-situ brecciation, rhizoconcretions, pisoids, alveolar-septa texture, and circumgranular cracks confirm the pedogenesis in both Nodular Limestone and Bryozoan Limestone formations. The conspicuous nodularity within the Nodular Limestone Formation relates to the pedogenetic process.

(c) The Bagh carbonate succession, comprising the Nodular Limestone and the Bryozoan Limestone, represents the upper part of a transgressive systems tract. The glauconite bed at the top of the Bryozoan Limestone Formation marks the boundary between overall transgressive Bagh Group and the prograding Lameta Formation.

(d) Isotope ratios of carbonate constituents within the Bagh Group, including bioclast, micrite/microspar reveal a thorough diagenetic resetting. While the $\delta^{13}C$ ratios of

a few micrite samples in the Nodular Limestone Formation bear the original isotopic signatures of seawater during the Upper Cretaceous, all samples of the Bryozoan Limestone are thoroughly altered. Luminescence pattern and isotope ratios clearly distinguish between unaltered marine carbonates, and meteoric and burial diagenetic cements.

Compliance with ethical standards

References

Adabi MH, Zohdi A, Ghabeishavi A, Amiri-Bakhtiyar H (2008) Applications of nummulitids and other larger benthic foraminifera in depositional environment and sequence stratigraphy: an example from the Eocene deposits in Zagros Basin, SW Iran. Facies 54:499–512

Ahmad AHM, Akhtar K (1990) Clastic environments and facies of the Lower Cretaceous Narmada Basin, India. Cretac Res 11:175–190

Akhtar K, Khan DA (1997) A Tidal Island model for carbonate sedimentation: Karondia Limestone of Cretaceous Narmada basin, India. J Geol Soc India 50:481–489

Alonso-Zarza AM (1999) Initial stages of laminar calcrete formation by roots: examples from the Neogene of central Spain. Sediment Geol 126:177–191

Alonso-Zarza AM, Sanz ME, Calvo JP, Estévez P (1998) Calcified root cells in Miocene pedogenic carbonates of the Madrid Basin: evidence for the origin of Microcodium. Sediment Geol 116:81–97

Armstrong-Altrin JS, Lee YI, Verma SP, Worden RH (2009) Carbon, oxygen, and strontium isotope geochemistry of carbonate rocks of the Upper Miocene Kudankulam Formation, Southern India: implications for paleoenvironment and diagenesis. Geochem 69:45–60

Banerjee S, Bhattacharya SK, Sarkar S (2006) Carbon and oxygen isotope compositions of the carbonate facies in the Vindhyan Supergroup, central India. J Earth Syst Sci 115:113–134

Banerjee S, Bansal U, Thorat AV (2016a) A review on palaeogeographic implications and temporal variation in glaucony composition. J Palaeogeogr 5:43–71

Banerjee S, Bansal U, Pande K, Meena SS (2016b) Compositional variability of glauconites within the Upper Cretaceous Karai Shale Formation, Cauvery Basin, India: implications for evaluation of stratigraphic condensation. Sediment Geol 331:12–29

Banerjee S, Khanolkar S, Saraswati PK (2018) Facies and depositional settings of the Middle Eocene-Oligocene carbonates in Kutch. Geodin Acta 30:119–136

Banner JL, Hanson GN (1990) Calculation of simultaneous isotopic and trace element variations during water–rock interaction with applications to carbonate diagenesis. Geochim Cosmochim Acta 54:3123–3137

Bansal U, Banerjee S, Ruidas DK, Pande K (2018) Origin and geochemical characterization of the glauconites in the Upper Cretaceous Lameta Formation, central India. J Palaeogeogr 7:99–116

Bansal U, Banerjee S, Pande K, Ruidas DK (2019) Unusual seawater composition of the Late Cretaceous Tethys imprinted in glauconite of Narmada basin, central India. Geol Mag. https://doi.org/10.1017/S0016756819000621

Bhattacharya B, Jha S (2014) Late Cretaceous diurnal tidal system: a study from Nimar Sandstone, Bagh Group, Narmada Valley, Central India. Curr Sci 107:1032–1037

Bhattacharya SK, Jani RA, Tripathi SC, Lahiri TC (1997) Carbon and oxygen isotopic compositions of Infratrappean Limestones from Central and Western India and their depositional environment. J Geol Soc India 50:289–296

Blanchet CL, Kasten S, Vidal L, Poulton SW, Ganeshram R, Thouveny N (2012) Influence of diagenesis on the stable isotopic composition of biogenic carbonates from the Gulf of Tehuantepec oxygen minimum zone. Geochem Geophys Geosyst 13:Q04003. https://doi.org/10.1029/2011GC003800

Boggs S Jr, Krinsley D (2006) Application of Cathodoluminescence Imaging to the Study of Sedimentary Rocks. Cambridge University Press, New York, pp 1–165

Bose PK, Das NG (1986) A trangressive storm–and fair–weather dominant shelf sequence, Cretaceous Nimar Formation, Chakrud, Madhya Pradesh, India. Sediment Geol 46:147–167

Bowen GJ, Wilkinson B (2002) Spatial distribution of $\delta^{18}O$ in meteoric precipitation. Geology 30:315–318

Brand U, Jiang GQ, Azmy K, Bishop J, Montañez IP (2012) Diagenetic evaluation of a Pennsylvanian carbonate succession (Bird Spring Formation, Arrow Canyon, Nevada, U.S.A.)—1: Brachiopod and whole rock comparison. Chem Geol 308–309:26–39

Budd DA, Gaswirth SB, Oliver WL (2002) Quantification of macroscopic subaerial exposure features in carbonate rocks. J Sediment Res 72:917–928

Buonocunto FP, Sprovieri M, Bellanca A, D'Argenio B, Ferreri V, Neri R, Ferruzza G (2002) Cyclostratigraphy and high-frequency carbon isotope fluctuations in Upper Cretaceous shallow-water carbonates, Southen Italy. Sedimentology 49:1321–1337

Burdett JW, Grotzinger JP, Arthur MA (1990) Did major changes in the stable–isotope composition of Proterozoic seawater occur? Geology 18:227–230

Calvet F, Julia R (1983) Pisoids in the caliche profiles of Tarragona NE Spain. In: Peryt TM (ed) Coated Grains. Springer-Verlag, Berlin, pp 456–473

Camoin GF (1993) Turonian and coniacian carbonate platforms from the African Tethyan Margin, Algeria, Tunisia. In: Simo JA, Scott RW and Masse J-P (eds). Cretaceous Carbonate Platforms, American Association of Petroleum Geologists, Memoir 56, pp 155–162

Chiplonkar GW (1937) Echinoids from the Bagh Beds. Proc Indian Acad Sci B 6:60–71

Chiplonkar GW, Badve RM (1976) Palaeontology ofthe Bagh Beds-Pt. IV. Inoceramidae. J Palaeontol Soc India 18:1–12

Coimbra R, Azerêdo AC, Cabral MC, Immenhauser A (2016) Palaeoenvironmental analysis of mid-Cretaceous coastal lagoonal deposits (Lusitanian Basin, W Portugal). Palaeogeogr Palaeoclimatol Palaeoecol 446:308–325

Coimbra R, Horikx M, Huck S, Heimhofer U, Immenhauser A, Rocha F, Dinis J, Duarte LV (2017) Statistical evaluation of elemental concentrations in shallow-marine deposits (Cretaceous, Lusitanian Basin). Mar Pet Geol 86:1029–1046

Colombie C, Strasser A (2005) Facies, cycles, and controls on the evolution of a keepup carbonate platform (Kimmeridgian, Swiss Jura). Sedimentology 52:1207–1227

Derry LA (2010) A burial diagenesis origin for the Ediacaran Shuram-Wonoka carbon isotope anomaly. Earth Planet Sci Lett 294:152–162

Dunham RJ (1969a) Early Vadose Silt in Townsend Mound Reef, New Mexico. SEPM Spec Publ 14(139):181

Dunham RJ (1969b) Vadose Pisolile in the Capitan Reef Permian, New Mexico and Texas. SEPM Spec Publ 14:182–191

Föllmi KB, Godet A (2013) Palaeoceanography of lower cretaceous alpine platform carbonates. Sedimentology 60:131–151

Flügel E (2004) Microfacies of Carbonate Rocks: Analysis Interpretation and Application. Springer-Verlag, Berlin, p 976

Fournier F, Montaggioni LF, Borgomano J (2004) Paleoenvironments and high-frequency cyclicity in the Cenozoic south-east Asian shallow-water carbonates: a case study from the Oligo-Miocene buildups of Malampaya (offshore Palawan, Philippines). Mar Pet Geol 21:1–22

Gangopadhyay TK, Halder K (1996) Significance of the first record of notiloid from the Upper Cretaceous Bagh group of rocks. Curr Sci 706:462–465

Gangopadhyay TK, Bardhan S (2000) Dimorphism and a new record of *Barroisiceras De Grossouvre* (Ammonoidea) from the Coniacian of Bagh, central India. Can J Earth Sci 37:1377–1387

Gilleaudeau GJ, Sahoo SK, Kah LC, Henderson MA, Kaufman AJ (2018) Proterozoic carbonates of the Vindhyan Basin, India: chemostratigraphy and diagenesis. Gondwana Res 57:10–25

Goldstein RH (1988) Paleosols of Late Pennsylvanian cyclic strata, New Mexico. Sedimentology 35:777–803

Gómez-Gras D, Alonso-Zarza M (2003) Reworked calcretes: their significance in the reconstruction of alluvial sequences (Permian and Triassic, Minorca, Balearic Islands, Spain). Sediment Geol 158:299–319

Guha AK (1975) Palaeoecology of the Bagh Group, Madhya Pradesh—an investigation based on Bryozoa. Indian J Earth Sci 22:190–201

Heba G, Prichonnet G, El Albani A (2009) Meteoric diagenesis of Upper Cretaceous and Paleocene–Eocene shallow-water carbonates in the Kruja platform (Albania): Geochemical evidence. Geol Carpath 60:165–179

Henderson A, Serra F, Feltes NA, Albanesi GL, Kah LC (2018) Paired isotope records of carbonate and organic matter from the Middle Ordovician of Argentina: intrabasinal variation and effects of the marine chemocline. Palaeogeogr Palaeoclimatol Palaeoecol 490:107–130

Hudson JD (1977) Stable isotopes and limestone lithification. J Geol Soc London 133:637–660

Jaitly AK, Ajane R (2013) Comments on Placenticeras mintoi Vredenburg, 1906 from the Bagh Beds Late Cretaceous, Central India with special reference to Turonian Nodular Limestone horizon. J Geol Soc India 81:565–574

James NP, Choquette PW (1990) Limestones: the meteoric diagenetic environment. Geosci Can Reprint Ser 4:35–73

Jarvis I, Trabucho-Alexandre J, Gröcke DR, Uličný D, Laurin J (2015) Intercontinental correlation of organic carbon and carbonate stable isotope records: evidence of climate and sea-level change during the Turonian (Cretaceous). Depos Rec 1:53–90

Jha S, Bhattacharya B, Nandwani S (2017) Significance of seismites in the Late Cretaceous transgressive Nimar Sandstone succession, Son-Narmada rift valley, central India. Geol J 52:768–783

Jaballah J, Negra MH (2016) Stratigraphical and sedimentary characters of Late Cretaceous formations outcropping in central and southern Tunisia, Tethyan southern margin. J Afr Earth Sci 124:289–310

Joachimski MM (1994) Subaerial exposure and deposition of shallowing upward sequences: evidence from stable isotopes of Purbeckian peritidal carbonates (basal Cretaceous), Swiss and French Jura Mountains. Sedimentology 41:805–824

Kennedy WJ, Phansalkar VG, Walaszczyk I (2003) *Prionocyclus germari* (Reuss, 1845), a Late Turonian marker fossil from the Bagh Beds of central India. Cretac Res 24:433–438

Kraus MJ, Hasiotis ST (2006) Significance of different modes of rhizolith preservation to interpreting paleoenvironmental and paleohydrologic settings: examples from paleogene paleosols, bighorn basin, wyoming, U.S.A. J Sediment Res 76:633–646

Kumar S, Pathak DB, Pandey B, Jaitly AK, Gautam JP (2018) The age of the Nodular Limestone Formation (Late Cretaceous), Narmada Basin, central India. J Earth Syst Sci 127:109. https://doi.org/10.1007/S12040-018-1017-1

Machel HG (2000) Application of cathodoluminescence to carbonate diagenesis. In: Pagel M, Barbin V, Blanc P, Ohnenstetter D (eds) Cathodoluminescence in Geosciences. Springer-Verlag, Berlin, pp 271–301

Machel HG, Mason RA, Mariano AN, Mucci A (1991) Causes and emission of luminescence in calcite and dolomite. In: Barker CE, Kopp OC (eds) Luminescence Microscopy and Spectroscopy: Qualitative and Quantitative Applications. SEPM Short Course Notes 25: 9–25

Magaritz M, Rahner S, Yechieli Y, Krishnamurthy RV (1991) 13C/12C ratio in organic matter from the Dead Sea area: paleoclimatic interpretation. Naturwissenschaften 78:453–455

Major RP (1991) Cathodoluminescence in Post-Miocene carbonates. In: Barker CE, Kopp OC (eds) Luminescence Microscopy and Spectroscopy: Qualitative and Quantitative Applications. SEPM Short Course Notes 25: 149–153

Martin-Chivelet J, Giménez R (1992) Paleosols in microtidal carbonate sequences. Sierra de Utiel Formation, Upper Cretaceous, SE Spain. Sediment Geol 81:125–145

Meyers WJ and Lohmann KC (1985) Isotope geochemistry of regionally extensive calcite cement zones and marine components in Mississippian limestones, New Mexico. In: Schneidermann N and Harris PM (eds) Carbonate Cements, SEPM Special Publications 26: 223–239

Moore CH (2001) Carbonate reservoir porosity evolution and diagenesis in a sequence–stratigraphic framework. Amsterdam, Elsevier, Developments in Sedimentology 55, 460 p

Pomoni-Papaioannou F, Kostopoulou V (2008) Microfacies and cycle stacking pattern in Liassic peritidal carbonate platform strata, Gavrovo-Tripolitza platform, Peloponnesus, Greece. Facies 54:417–431

Pomoni-Papaioannou F, Zampetakis-Lekkas A (2009) Facies associations of the late Cenomanian carbonate platform of Tripolitza subzone Vitina, Central Peloponnesus, Greece: evidence of long-term/terrestrial subaerial exposure. Italian J Geosci 128:123–130

Pomoni-Papaioannou F, Karakitsios V (2016) Sedimentary facies analysis of a high-frequency, small-scale, peritidal carbonate sequence in the Lower Jurassic of the Tripolis carbonate unit central western Crete, Greece: Long-lasting emergence and fossil laminar dolocretes horizons. J Palaeogeogr 53:241–257

Racey A, Fisher J, Bailey H, Roy SK (2016) The value of fieldwork in making connections between onshore outcrops and offshore models: an example from India. In: Bowman M, Smyth HR, Good TR, Passey SR, Hirst JPP, Jordan CJ (eds) The value of outcrop studies in reducing subsurface uncertainty and risk in hydrocarbon exploration and production. Special Publication of the Geological Society of London 436 https://doi.org/10.1144/SP436.9

Rasser MW, Scheibner C, Mutti M (2005) A paleoenvironmental standard section for Early Ilerdian tropical carbonate factories (Corbieres, France; Pyrenees, Spain). Facies 51:217–232

Saller AH, Moore CH (1989) Meteoric diagenesis, marine diagenesis, and microporosity in Pleistocene and Oligocene limestones, Enewetak Atoll, Marshall Islands. Sediment Geol 63:253–272

Sanders D (1998) Upper Cretaceous 'rudist formations'. Geol Paläont Mitt Innsbruck 23:37–59

Sarkar S, Chakraborty N, Mandal A, Banerjee S, Bose PK (2014) Siliciclastic-carbonate mixing modes in the river-mouth bar palaeogeography of the Upper Cretaceous Garudamangalam Sandstone (Ariyalur, India). J Palaeogeogr 3:233–256

Sattler U, Immenhauser A, Hillgartner H, Esteban M (2005) Characterization, lateral variability and lateral extent of discontinuity surfaces on a carbonate platform (Barremian to Lower Aptian, Oman). Sedimentology 52:339–361

Scorrer S, Azmy K, Stouge S (2019) Carbon-isotope stratigraphy of the Furongian Berry Head Formation (Port au Port Group) and Tremadocian Watts Bight Formation (St. George Group), western Newfoundland, and the correlative significance. Can J Earth Sci 56:223–234

Sellwood BW (1993) Structure and origin of limestones. J Geol Soc London 150:801–809

Singh SK, Dayal RM (1979) Trace fossils and environment of deposition of Nimar Sandstone, Bagh Beds. J Geol Soc India 20:234–239

Singh SK, Srivastava HK (1981) Lithostratigraphy of Bagh Beds and its correlation with Lameta Beds. J Palaeontol Soc India 26:77–85

Singh IB, Shekhar S, Agarwal SC (1983) Palaeoenvironment and stratigraphic position of green sandstone Lameta: Late Cretaceous Jabalpur area. J Geol Soc India 24:412–420

Spence GH, Tucker ME (1997) Genesis of limestone megabreccias and their significance in sequence stratigraphic models. Sediment Geol 112:163–193

Strasser A (1991) Lagoonal–peritidal sequences in carbonate environments: autocyclic and allocyclic processes. In: Einsele G, Ricken W, Seilacher A (eds) Cycles and Events in Stratigraphy, Springer–Verlag, pp 709–721

Tandon SK (2000) Spatio–temporal patterns of environmental changes in Late Cretaceous sequences of central India. In: Okada H, Mateer NJ (eds) Cretaceous Environments of Asia, vol 17. Elsevier, Amsterdam, pp 225–241

Tripathi SC (1995) Palaeontological and Palaeoenvironmental studies of Bagh Group, M.P. Rec Geol Surv India 128:104–105

Tripathi SC (2006) Geology and evolution of the Cretaceous infratrappean basins of Lower Narmada Valley, western India. J Geol Soc India 674:459–468

Tripathi SC, Lahiri TC (2000) Marine oscillation event stratification: an example from Late Cretaceous Bagh carbonates sequence of Narmada valley, India. Mem Geol Soc India 46:15–24

Tucker ME, Wright VP (1990) Carbonate sedimentology. Blackwell Scientific, Oxford, p 482

Vincent B, Rambeau C, Emmanuel L, Loreau J-P (2006) Sedimentology and trace element geochemistry of shallow-marine carbonates: an approach to paleoenvironmental analysis along the Pagny-sur-Meuse Section (Upper Jurassic, France). Facies 52:69–84

Wendler I (2013) A critical evaluation of carbon isotope stratigraphy and biostratigraphic implications for Late Cretaceous global correlation. Earth Sci Rev 126:116–146

Wilmsen M, Berensmeier M, Fürsich TT, Majidifard MR, Schlagintweit F (2018) A Late Cretaceous epeiric carbonate platform: the Haftoman Formation of Central Iran. Facies 64:11. https://doi.org/10.1007/s10347-018-0523-6

Wilson MEJ, Evans MJ (2002) Sedimentology and diagenesis of tertiary carbonates on the Mangkalihat Peninsula, Borneo: implications for subsurface reservoir quality. Mar Pet Geol 19:873–900

Wright VP (1994) Paleosols in shallow marine carbonate sequences. Earth Sci Rev 35:367–395

Zampetakis-Lekkas A, Pomoni-Papaioannou F, Alexopoulos A (2007) New stratigraphic and palaeogeographic data from the Mesozoic strata of the Tripolitza platform in Central Crete. Evidence of subaerial exposures during Albian-Early Cenomanian. Hell J Geosci 42:7–18